**PAPER • OPEN ACCESS**

# Sub-percent precision measurement of neutrino oscillation parameters with JUNO[*]

To cite this article: Angel Abusleme *et al* 2022 *Chinese Phys. C* **46** 123001

View the article online for updates and enhancements.

# Sub-percent precision measurement of neutrino oscillation parameters with JUNO[*]

Angel Abusleme[5,41]    Thomas Adam[46]    Shakeel Ahmad[67]    Rizwan Ahmed[67]    Sebastiano Aiello[56]

Muhammad Akram[67]    Abid Aleem[67]    Fengpeng An(安丰鹏)[29]    Qi An(安琪)[22]    Giuseppe Andronico[56]

Nikolay Anfimov[68]    Vito Antonelli[58]    Tatiana Antoshkina[68]    Burin Asavapibhop[72]

João Pedro Athayde Marcondes de André[46]    Didier Auguste[44]    Weidong Bai(白伟东)[20]    Nikita Balashov[68]

Wander Baldini[57]    Andrea Barresi[59]    Davide Basilico[58]    Eric Baussan[46]    Marco Bellato[61]    Antonio Bergnoli[61]

Thilo Birkenfeld[49]    Sylvie Blin[44]    David Blum[55]    Simon Blyth[10]    Anastasia Bolshakova[68]    Mathieu Bongrand[48]

Clément Bordereau[45,40]    Dominique Breton[44]    Augusto Brigatti[58]    Riccardo Brugnera[62]    Riccardo Bruno[56]

Antonio Budano[65]    Jose Busto[47]    Ilya Butorov[68]    Anatael Cabrera[44]    Barbara Caccianiga[58]    Hao Cai(蔡浩)[34]

Xiao Cai(蔡啸)[10]    Yanke Cai(蔡严克)[10]    Zhiyan Cai(蔡志岩)[10]    Riccardo Callegari[62]    Antonio Cammi[60]

Agustin Campeny[5,41]    Chuanya Cao(曹传亚)[10]    Guofu Cao(曹国富)[10]    Jun Cao(曹俊)[10]    Rossella Caruso[56]

Cédric Cerna[45]    Chi Chan[38]    Jinfan Chang(常劲帆)[10]    Yun Chang[39]    Guoming Chen(陈国明)[28]

Pingping Chen(陈平平)[18]    Po-An Chen[40]    Shaomin Chen(陈少敏)[13]    Xurong Chen[26]    Yixue Chen(陈义学)[11]

Yu Chen(陈羽)[20]    Zhiyuan Chen(陈志源)[10]    Zikang Chen(陈梓康)[20]    Jie Cheng(程捷)[11]    Yaping Cheng(程雅苹)[7]

Yu Chin Cheng[40]    Alexey Chetverikov[68]    Davide Chiesa[59]    Pietro Chimenti[3]    Artem Chukanov[68]    Gérard Claverie[45]

Catia Clementi[63]    Barbara Clerbaux[2]    Selma Conforti Di Lorenzo[45]    Daniele Corti[61]    Flavio Dal Corso[61]

Olivia Dalager[75]    Christophe De La Taille[45]    Zhi Deng(邓智)[13]    Ziyan Deng(邓子艳)[10]    Wilfried Depnering[52]

Marco Diaz[5]    Xuefeng Ding[58]    Yayun Ding(丁雅韵)[10]    Bayu Dirgantara[74]    Sergey Dmitrievsky[68]    Tadeas Dohnal[42]

Dmitry Dolzhikov[68]    Georgy Donchenko[70]    Jianmeng Dong(董建蒙)[13]    Evgeny Doroshkevich[69]    Marcos Dracos[46]

Frédéric Druillole[45]    Ran Du(杜然)[10]    Shuxian Du(杜书先)[37]    Stefano Dusini[61]    Martin Dvorak[42]    Timo Enqvist[43]

Heike Enzmann[52]    Andrea Fabbri[65]    Donghua Fan[24]    Lei Fan(樊磊)[10]    Jian Fang(方建)[10]    Wenxing Fang(方文兴)[10]

Marco Fargetta[56]    Dmitry Fedoseev[68]    Zhengyong Fei(费政勇)[10]    Li-Cheng Feng[38]    Qichun Feng(冯启春)[21]

Richard Ford[58]    Amélie Fournier[45]    Haonan Gan(甘浩男)[32]    Feng Gao(高峰)[49]    Alberto Garfagnini[62]

Arsenii Gavrikov[68]    Marco Giammarchi[58]    Nunzio Giudice[56]    Maxim Gonchar[68]    Guanghua Gong(龚光华)[13]

Hui Gong(宫辉)[13]    Yuri Gornushkin[68]    Alexandre Göttel[51,49]    Marco Grassi[62]    Vasily Gromov[68]

Minghao Gu(顾旻皓)[10]    Xiaofei Gu(谷肖飞)[37]    Yu Gu(古宇)[19]    Mengyun Guan(关梦云)[10]    Yuduo Guan(管宇铎)[10]

Nunzio Guardone[56]    Cong Guo(郭聪)[10]    Jingyuan Guo(郭竞渊)[20]    Wanlei Guo(郭万磊)[10]    Xinheng Guo[8]

Yuhang Guo(郭宇航)[35]    Paul Hackspacher[52]    Caren Hagner[50]    Ran Han(韩然)[7]    Yang Han[20]    Miao He(何苗)[10]

Wei He[10]    Tobias Heinz[55]    Patrick Hellmuth[45]    Yuekun Heng(衡月昆)[10]    Rafael Herrera[5,41]

YuenKeung Hor(贺远强)[20]    Shaojing Hou(侯少静)[10]    Yee Hsiung[40]    Bei-Zhen Hu[40]    Hang Hu(胡航)[20]

Jianrun Hu[10]    Jun Hu(胡俊)[10]    Shouyang Hu(胡守扬)[9]    Tao Hu(胡涛)[10]    Yuxiang Hu(胡宇翔)[10]

Zhuojun Hu(胡焯钧)[20]    Guihong Huang(黄桂鸿)[24]    Hanxiong Huang(黄翰雄)[9]    Kaixuan Huang(黄凯旋)[20]

Wenhao Huang(黄文昊)[25]  Xin Huang[10]  Xingtao Huang(黄性涛)[25]  Yongbo Huang(黄永波)[28]  Jiaqi Hui(惠加琪)[30]

Lei Huo(霍雷)[21]  Wenju Huo(霍文驹)[22]  Cédric Huss[45]  Safeer Hussain[67]  Ara Ioannisian[1]  Roberto Isocrate[61]

Beatrice Jelmini[62]  Ignacio Jeria[5]  Xiaolu Ji(季筱璐)[10]  Huihui Jia(贾慧慧)[33]  Junji Jia(贾俊基)[34]

Siyu Jian(蹇司玉)[9]  Di Jiang(蒋荻)[22]  Wei Jiang(蒋炜)[10]  Xiaoshan Jiang(江晓山)[10]  Xiaoping Jing(荆小平)[10]

Cécile Jollet[45]  Jari Joutsenvaara[43]  Leonidas Kalousis[46]  Philipp Kampmann[54,51]  Li Kang(康丽)[18]

Rebin Karaparambil[48]  Narine Kazarian[1]  Amina Khatun[71]  Khanchai Khosonthongkee[74]  Denis Korablev[68]

Konstantin Kouzakov[70]  Alexey Krasnoperov[68]  Nikolay Kutovskiy[68]  Pasi Kuusiniemi[43]  Tobias Lachenmaier[55]

Cecilia Landini[58]  Sébastien Leblanc[45]  Victor Lebrin[48]  Frederic Lefevre[48]  Ruiting Lei(雷瑞庭)[18]  Rupert Leitner[42]

Jason Leung[38]  Daozheng Li[10]  Demin Li(李德民)[37]  Fei Li(李飞)[10]  Fule Li(李福乐)[13]  Gaosong Li(李高嵩)[10]

Huiling Li[10]  Mengzhao Li(李梦朝)[10]  Min Li(李民)[10]  Nan Li(李楠)[10]  Nan Li[16]  Qingjiang Li(李清江)[16]

Ruhui Li(李茹慧)[10]  Rui Li(李瑞)[30]  Shanfeng Li(黎山峰)[18]  Tao Li(李涛)[20]  Teng Li(李腾)[25]

Weidong Li(李卫东)[10,14]  Weiguo Li(李卫国)[10]  Xiaomei Li(李笑梅)[9]  Xiaonan Li(李小男)[10]  Xinglong Li(李兴隆)[9]

Yi Li(李仪)[18]  Yichen Li(李依宸)[10]  Yufeng Li(李玉峰)[10]  Zepeng Li[10]  Zhaohan Li(李兆涵)[10]

Zhibing Li(李志兵)[20]  Ziyuan Li(李紫源)[20]  Zonghai Li(李宗海)[34]  Hao Liang(梁浩)[9]  Hao Liang(梁昊)[22]

Jiajun Liao(廖佳军)[20]  Ayut Limphirat[74]  Guey-Lin Lin[38]  Shengxin Lin(林盛鑫)[18]  Tao Lin(林韬)[10]

Jiajie Ling(凌家杰)[20]  Ivano Lippi[61]  Fang Liu(刘芳)[11]  Haidong Liu(刘海东)[37]  Haotian Liu(刘昊天)[34]

Hongbang Liu(刘宏邦)[28]  Hongjuan Liu(刘红娟)[23]  Hongtao Liu(刘洪涛)[20]  Hui Liu[19]  Jianglai Liu(刘江来)[30,31]

Jinchang Liu(刘金昌)[10]  Min Liu(刘敏)[23]  Qian Liu(刘倩)[14]  Qin Liu(刘钦)[22]  Runxuan Liu[51,49]

Shubin Liu(刘树彬)[22]  Shulin Liu(刘术林)[10]  Xiaowei Liu(刘小伟)[20]  Xiwen Liu(刘熙文)[28]  Yan Liu[10]

Yunzhe Liu[10]  Alexey Lokhov[70,69]  Paolo Lombardi[58]  Claudio Lombardo[56]  Kai Loo[52]  Chuan Lu(陆川)[32]

Haoqi Lu(路浩奇)[10]  Jingbin Lu(陆景彬)[15]  Junguang Lu(吕军光)[10]  Shuxiang Lu(路书祥)[37]

Bayarto Lubsandorzhiev[69]  Sultim Lubsandorzhiev[69]  Livia Ludhova[51,49]  Arslan Lukanov[69]  Daibin Luo[10]

Fengjiao Luo[23]  Guang Luo(罗光)[20]  Shu Luo(罗舒)[36]  Wuming Luo(罗武鸣)[10]  Xiaojie Luo(罗晓杰)[10]

Vladimir Lyashuk[69]  Bangzheng Ma(马帮争)[25]  Bing Ma(马冰)[37]  Qiumei Ma(马秋梅)[10]  Si Ma(马斯)[10]

Xiaoyan Ma(马骁妍)[10]  Xubo Ma(马续波)[11]  Jihane Maalmi[44]  Jingyu Mai(麦景宇)[20]  Yury Malyshkin[68]

Roberto Carlos Mandujano[75]  Fabio Mantovani[57]  Francesco Manzali[62]  Xin Mao(冒鑫)[7]  Yajun Mao(冒亚军)[12]

Stefano M. Mari[65]  Filippo Marini[62]  Cristina Martellini[65]  Gisele Martin-Chassard[44]  Agnese Martini[64]

Matthias Mayer[53]  Davit Mayilyan[1]  Ints Mednieks[66]  Artur Meinusch[52]  Yue Meng(孟月)[30]  Anselmo Meregaglia[45]

Emanuela Meroni[58]  David Meyhö[50]  Mauro Mezzetto[61]  Jonathan Miller[6]  Lino Miramonti[58]

Marta Colomer Molla[2]  Paolo Montini[65]  Michele Montuschi[57]  Axel Müller[55]  Massimiliano Nastasi[59]  Dmitry
V. Naumov[68]  Elena Naumova[68]  Diana Navas-Nicolas[44]  Igor Nemchenok[68]  Minh Thuan Nguyen Thi[38]

Feipeng Ning(宁飞鹏)[10]  Zhe Ning(宁哲)[10]  Hiroshi Nunokawa[4]  Lothar Oberauer[53]  Juan Pedro Ochoa-Ricoux[75,5,41]

Alexander Olshevskiy[68]  Domizia Orestano[65]  Fausto Ortica[63]  Rainer Othegraven[52]  Alessandro Paoloni[64]

Sergio Parmeggiano[58]  Yatian Pei(裴亚田)[10]  Luca Pelicci[51,49]  Nicomede Pelliccia[63]  Anguo Peng(彭安国)[23]

Haiping Peng(彭海平)[22]  Yu Peng(彭宇)[10]  Zhaoyuan Peng(彭昭缘)[10]  Frédéric Perrot[45]  Pierre-Alexandre Petitjean[2]

Fabrizio Petrucci[65]  Oliver Pilarczyk[52]  Luis Felipe Piñeres[46]  Artyom Popov[70]  Pascal Poussot[46]  Ezio Previtali[59]

Fazhi Qi(齐法制)[10]  Ming Qi(祁鸣)[27]  Sen Qian(钱森)[10]  Xiaohui Qian(钱小辉)[10]  Zhen Qian(钱圳)[20]

Hao Qiao(乔浩)[12]  Zhonghua Qin(秦中华)[10]  Shoukang Qiu(丘寿康)[23]  Gioacchino Ranucci[58]  Neill Raper[20]

Reem Rasheed[45]  Alessandra Re[58]  Henning Rebber[50]  Abdel Rebii[45]  Mariia Redchuk[61]  Bin Ren(任斌)[18]

Jie Ren(任杰)[9]  Barbara Ricci[57]  Mariam Rifai[51,49]  Mathieu Roche[45]  Narongkiat Rodphai[72]  Aldo Romani[63]

Bedřich Roskovec[42]  Xichao Ruan(阮锡超)[9]  Arseniy Rybnikov[68]  Andrey Sadovsky[68]  Paolo Saggese[58]

Simone Sanfilippo[65]  Anut Sangka[73]  Utane Sawangwit[73]  Julia Sawatzki[53]  Michaela Schever[51,49]  Cédric Schwab[46]

Konstantin Schweizer[53]  Alexandr Selyunin[68]  Andrea Serafini[62]  Giulio Settanta[51#]  Mariangela Settimo[48]

Zhuang Shao[35]  Vladislav Sharov[68]  Arina Shaydurova[68]  Jingyan Shi(石京燕)[10]  Yanan Shi(史娅楠)[10]

Vitaly Shutov[68]  Andrey Sidorenkov[69]  Fedor Šimkovic[71]  Chiara Sirignano[62]  Jaruchit Siripak[74]  Monica Sisti[59]

Maciej Slupecki[43]  Mikhail Smirnov[20]  Oleg Smirnov[68]  Thiago Sogo-Bezerra[48]  Sergey Sokolov[68]

Julanan Songwadhana[74]    Boonrucksar Soonthornthum[73]    Albert Sotnikov[68]    Ondřej Šrámek[42]

Warintorn Sreethawong[74]    Achim Stahl[49]    Luca Stanco[61]    Konstantin Stankevich[70]    Dušan Štefánik[71]

Hans Steiger[52,53]    Jochen Steinmann[49]    Tobias Sterr[55]    Matthias Raphael Stock[53]    Virginia Strati[57]

Alexander Studenikin[70]    Jun Su(苏俊)[20]    Shifeng Sun(孙世峰)[11]    Xilei Sun(孙希磊)[10]    Yongjie Sun(孙勇杰)[22]

Yongzhao Sun(孙永昭)[10]    Zhengyang Sun(孙正阳)[30]    Narumon Suwonjandee[72]    Michal Szelezniak[46]

Jian Tang(唐健)[20]    Qiang Tang(唐强)[20]    Quan Tang(唐泉)[23]    Xiao Tang(唐晓)[10]    Vidhya Thara Hariharan[50]

Eric Theisen[52]    Alexander Tietzsch[55]    Igor Tkachev[69]    Tomas Tmej[42]    Marco Danilo Claudio Torri[58]

Konstantin Treskov[68]    Andrea Triossi[62]    Giancarlo Troni[5]    Wladyslaw Trzaska[43]    Alexandros Tsagkarakis[49]

Cristina Tuve[56]    Nikita Ushakov[69]    Vadim Vedin[66]    Giuseppe Verde[56]    Maxim Vialkov[70]    Benoit Viaud[48]

Cornelius Moritz Vollbrecht[51,49]    Cristina Volpe[44]    Katharina Von Sturm[62]    Vit Vorobel[42]    Dmitriy Voronin[69]

Lucia Votano[64]    Pablo Walker[5,41]    Caishen Wang(王彩申)[18]    Chung-Hsiang Wang[39]    En Wang(王恩)[37]

Guoli Wang(王国利)[21]    Jian Wang(王坚)[22]    Jun Wang(王俊)[20]    Lu Wang(汪璐)[10]    Meifen Wang[10]

Meng Wang(王孟)[23]    Meng Wang[25]    Ruiguang Wang(王瑞光)[10]    Siguang Wang(王思广)[12]    Wei Wang(王维)[27]

Wei Wang(王为)[20]    Wenshuai Wang(王文帅)[10]    Xi Wang(王玺)[16]    Xiangyue Wang(王湘粤)[20]

Yangfu Wang(王仰夫)[10]    Yaoguang Wang(王耀光)[10]    Yi Wang(王毅)[13]    Yi Wang(王义)[24]    Yifang Wang(王贻芳)[10]

Yuanqing Wang(王元清)[13]    Yuman Wang[27]    Zhe Wang(王喆)[13]    Zheng Wang(王铮)[10]    Zhimin Wang(王志民)[10]

Zongyi Wang[13]    Apimook Watcharangkool[73]    Wei Wei(魏微)[10]    Wei Wei(魏巍)[25]    Wenlu Wei(韦雯露)[10]

Yadong Wei(魏亚东)[18]    Kaile Wen(温凯乐)[10]    Liangjian Wen(温良剑)[10]    Christopher Wiebusch[49]

Steven Chan-Fai Wong(黄振辉)[20]    Bjoern Wonsak[50]    Diru Wu(吴帝儒)[10]    Qun Wu(吴群)[25]    Zhi Wu(吴智)[10]

Michael Wurm[52]    Jacques Wurtz[46]    Christian Wysotzki[49]    Yufei Xi(习宇飞)[32]    Dongmei Xia(夏冬梅)[17]

Xiang Xiao[20]    Xiaochuan Xie(谢小川)[28]    Yuguang Xie(谢宇广)[10]    Zhangquan Xie[10]    Zhao Xin(辛钊)[10]

Zhizhong Xing(邢志忠)[10]    Benda Xu(续本达)[13]    Cheng Xu(徐程)[23]    Donglian Xu(徐东莲)[31,30]

Fanrong Xu(徐繁荣)[19]    Hangkun Xu(许杭锟)[10]    Jilei Xu(徐吉磊)[10]    Jing Xu(徐晶)[8]    Meihang Xu(徐美杭)[10]

Yin Xu(徐音)[33]    Baojun Yan(闫保军)[10]    Taylor Yan[74]    Wenqi Yan[10]

Xiongbo Yan(严雄波)[10]    Yupeng Yan[74]    Changgen Yang(杨长根)[10]    Chengfeng Yang(杨成峰)[28]    Huan Yang[10]

Jie Yang(杨洁)[37]    Lei Yang(杨雷)[18]    Xiaoyu Yang(杨晓宇)[10]    Yifan Yang[10]    Yifan Yang[2]    Haifeng Yao(姚海峰)[10]

Jiaxuan Ye(叶佳璇)[10]    Mei Ye(叶梅)[10]    Ziping Ye(叶子平)[31]    Frédéric Yermia[48]    Na Yin[25]

Zhengyun You(尤郑昀)[20]    Boxiang Yu(俞伯祥)[10]    Chiye Yu(余炽业)[18]    Chunxu Yu(喻纯旭)[33]

Hongzhao Yu(余泓钊)[20]    Miao Yu(于淼)[34]    Xianghui Yu(于向辉)[33]    Zeyuan Yu(于泽源)[10]    Zezhong Yu(于泽众)[10]

Cenxi Yuan(袁岑溪)[20]    Chengzhuo Yuan(袁成卓)[10]    Ying Yuan(袁影)[12]    Zhenxiong Yuan(袁振雄)[13]

Baobiao Yue(岳保彪)[20]    Noman Zafar[67]    Vitalii Zavadskyi[68]    Shan Zeng(曾珊)[10]    Tingxuan Zeng(曾婷轩)[10]

Yuda Zeng(曾裕达)[20]    Liang Zhan(占亮)[10]    Aiqiang Zhang(张爱强)[13]    Bin Zhang(张斌)[37]    Binting Zhang(张斌婷)[10]

Feiyang Zhang(张飞洋)[30]    Guoqing Zhang[10]    Honghao Zhang(张宏浩)[20]    Jialiang Zhang(张家梁)[27]

Jiawen Zhang(张家文)[10]    Jie Zhang(张杰)[10]    Jin Zhang[28]    Jingbo Zhang(张景波)[21]    Jinnan Zhang(张金楠)[10]

Mohan Zhang[10]    Peng Zhang(张鹏)[10]    Qingmin Zhang(张清民)[35]    Shiqi Zhang(张石其)[20]    Shu Zhang(张澍)[20]

Tao Zhang(张涛)[30]    Xiaomei Zhang(张晓梅)[10]    Xin Zhang(张鑫)[10]    Xuantong Zhang(张玄同)[10]    Xueyao Zhang[25]

Yinhong Zhang(张银鸿)[10]    Yiyu Zhang(张易于)[10]    Yongpeng Zhang(张永鹏)[10]    Yu Zhang(张宇)[10]

Yuanyuan Zhang(张圆圆)[30]    Yumei Zhang(张玉美)[20]    Zhenyu Zhang(张振宇)[34]    Zhijian Zhang(张志坚)[18]

Fengyi Zhao[26]    Jie Zhao(赵洁)[10]    Rong Zhao(赵荣)[20]    Runze Zhao(赵润泽)[10]    Shujun Zhao(赵书俊)[37]

Dongqin Zheng[19]    Hua Zheng(郑华)[18]    Yangheng Zheng(郑阳恒)[14]    Weirong Zhong[19]    Jing Zhou(周静)[9]

Li Zhou(周莉)[10]    Nan Zhou(周楠)[22]    Shun Zhou(周顺)[10]    Tong Zhou(周彤)[10]    Xiang Zhou(周详)[34]

Jiang Zhu(朱江)[20]    Jingsen Zhu(朱景森)[29]    Kangfu Zhu(朱康甫)[35]    Kejun Zhu(朱科军)[10]    Zhihang Zhu(朱志航)[10]

Bo Zhuang(庄博)[10]    Honglin Zhuang(庄红林)[10]    Liang Zong(宗亮)[13]    Jiaheng Zou(邹佳恒)[10]

(JUNO Collaboration)

[1]Yerevan Physics Institute, Yerevan, Armenia
[2]Universié Libre de Bruxelles, Brussels, Belgium
[3]Universidade Estadual de Londrina, Londrina, Brazil

[4]Pontificia Universidade Catolica do Rio de Janeiro, Rio de Janeiro, Brazil
[5]Pontificia Universidad Católica de Chile, Santiago, Chile
[6]Universidad Tecnica Federico Santa Maria, Valparaiso, Chile
[7]Beijing Institute of Spacecraft Environment Engineering, Beijing, China
[8]Beijing Normal University, Beijing, China
[9]China Institute of Atomic Energy, Beijing, China
[10]Institute of High Energy Physics, Beijing, China
[11]North China Electric Power University, Beijing, China
[12]School of Physics, Peking University, Beijing, China
[13]Tsinghua University, Beijing, China
[14]University of Chinese Academy of Sciences, Beijing, China
[15]Jilin University, Changchun, China
[16]College of Electronic Science and Engineering, National University of Defense Technology, Changsha, China
[17]Chongqing University, Chongqing, China
[18]Dongguan University of Technology, Dongguan, China
[19]Jinan University, Guangzhou, China
[20]Sun Yat-Sen University, Guangzhou, China
[21]Harbin Institute of Technology, Harbin, China
[22]University of Science and Technology of China, Hefei, China
[23]The Radiochemistry and Nuclear Chemistry Group in University of South China, Hengyang, China
[24]Wuyi University, Jiangmen, China
[25]Shandong University, Jinan, China, and Key Laboratory of Particle Physics and Particle Irradiation of Ministry of Education, Shandong University, Qingdao, China
[26]Institute of Modern Physics, Chinese Academy of Sciences, Lanzhou, China
[27]Nanjing University, Nanjing, China
[28]Guangxi University, Nanning, China
[29]East China University of Science and Technology, Shanghai, China
[30]School of Physics and Astronomy, Shanghai Jiao Tong University, Shanghai, China
[31]Tsung-Dao Lee Institute, Shanghai Jiao Tong University, Shanghai, China
[32]Institute of Hydrogeology and Environmental Geology, Chinese Academy of Geological Sciences, Shijiazhuang, China
[33]Nankai University, Tianjin, China
[34]Wuhan University, Wuhan, China
[35]Xi'an Jiaotong University, Xi'an, China
[36]Xiamen University, Xiamen, China
[37]School of Physics and Microelectronics, Zhengzhou University, Zhengzhou, China
[38]Institute of Physics, National Yang Ming Chiao Tung University, Hsinchu
[39]National United University, Miao-Li
[40]Department of Physics, National Taiwan University, Taipei
[41]Millennium Institute for SubAtomic Physics at the High-energy Frontier (SAPHIR), Chile
[42]Charles University, Faculty of Mathematics and Physics, Prague, Czech Republic
[43]University of Jyvaskyla, Department of Physics, Jyvaskyla, Finland
[44]IJCLab, Universié Paris-Saclay, CNRS/IN2P3, 91405 Orsay, France
[45]Univ. Bordeaux, CNRS, LP2i Bordeaux, UMR 5797, F-33170 Gradignan, France
[46]IPHC, Universié de Strasbourg, CNRS/IN2P3, F-67037 Strasbourg, France
[47]Centre de Physique des Particules de Marseille, Marseille, France
[48]SUBATECH, Nantes Universié , IMT Atlantique, CNRS-IN2P3, Nantes, France
[49]III. Physikalisches Institut B, RWTH Aachen University, Aachen, Germany
[50]Institute of Experimental Physics, University of Hamburg, Hamburg, Germany
[51]Forschungszentrum Jülich GmbH, Nuclear Physics Institute IKP-2, Jülich, Germany
[52]Institute of Physics and EC PRISMA$^+$, Johannes Gutenberg Universität Mainz, Mainz, Germany
[53]Technische Universität München, München, Germany
[54]GSI Helmholtzzentrum für Schwerionenforschung, Planckstrasse 1, D-64291 Darmstadt, Germany
[55]Eberhard Karls Universität Tübingen, Physikalisches Institut, Tübingen, Germany
[56]INFN Catania and Dipartimento di Fisica e Astronomia dell´Università di Catania, Catania, Italy
[57]Department of Physics and Earth Science, University of Ferrara and INFN Sezione di Ferrara, Ferrara, Italy
[58]INFN Sezione di Milano and Dipartimento di Fisica dell´Università di Milano, Milano, Italy
[59]INFN Milano Bicocca and University of Milano Bicocca, Milano, Italy
[60]INFN Milano Bicocca and Politecnico of Milano, Milano, Italy
[61]INFN Sezione di Padova, Padova, Italy
[62]Dipartimento di Fisica e Astronomia dell'Università di Padova and INFN Sezione di Padova, Padova, Italy
[63]INFN Sezione di Perugia and Dipartimento di Chimica, Biologia e Biotecnologie dell'Università di Perugia, Perugia, Italy
[64]Laboratori Nazionali di Frascati dell'INFN, Roma, Italy
[65]University of Roma Tre and INFN Sezione Roma Tre, Roma, Italy
[66]Institute of Electronics and Computer Science, Riga, Latvia
[67]Pakistan Institute of Nuclear Science and Technology, Islamabad, Pakistan
[68]Joint Institute for Nuclear Research, Dubna, Russia
[69]Institute for Nuclear Research of the Russian Academy of Sciences, Moscow, Russia
[70]Lomonosov Moscow State University, Moscow, Russia

[71]Comenius University Bratislava, Faculty of Mathematics, Physics and Informatics, Bratislava, Slovakia
[72]Department of Physics, Faculty of Science, Chulalongkorn University, Bangkok, Thailand
[73]National Astronomical Research Institute of Thailand, Chiang Mai, Thailand
[74]Suranaree University of Technology, Nakhon Ratchasima, Thailand
[75]Department of Physics and Astronomy, University of California, Irvine, California, USA
[#]Now at Istituto Superiore per la Protezione e la Ricerca Ambientale, Via Vitaliano Brancati, 48, 00144 Roma, Italy

**Abstract:** JUNO is a multi-purpose neutrino observatory under construction in the south of China. This publication presents new sensitivity estimates for the measurement of the $\Delta m_{31}^2$, $\Delta m_{21}^2$, $\sin^2\theta_{12}$, and $\sin^2\theta_{13}$ oscillation parameters using reactor antineutrinos, which is one of the primary physics goals of the experiment. The sensitivities are obtained using the best knowledge available to date on the location and overburden of the experimental site, the nuclear reactors in the surrounding area and beyond, the detector response uncertainties, and the reactor antineutrino spectral shape constraints expected from the TAO satellite detector. It is found that the $\Delta m_{21}^2$ and $\sin^2\theta_{12}$ oscillation parameters will be determined to 0.5% precision or better in six years of data collection. In the same period, the $\Delta m_{31}^2$ parameter will be determined to about 0.2% precision for each mass ordering hypothesis. The new precision represents approximately an order of magnitude improvement over existing constraints for these three parameters.

## I. INTRODUCTION

Neutrinos have provided us with the first direct evidence of physics beyond the Standard Model (SM) of elementary particles, and the study of their properties stands as one of the most active directions within particle physics. First detected by Reines and Cowan in 1956 [1], these particles were discovered to oscillate roughly four decades later [2, 3], an unambiguous sign that they are massive and that the SM needs to be modified.

The phenomenology of neutrino oscillations granted elegant solutions to the solar neutrino [4] and atmospheric neutrino [5] anomalies through the transformation of electron and muon neutrinos into other neutrino flavors, respectively. To date, almost all neutrino data collected with accelerator, solar, atmospheric, and reactor neutrinos [6] can be explained within the standard three-neutrino oscillation paradigm that will be described in the next section. It is essential, however, that the accuracy of this paradigm be scrutinized with increasing precision to inform future experiments, provide important constraints to model building, and probe for other physics beyond the SM.

### A. Neutrino masses and mixing

In the standard three neutrino flavor scheme, neutrino oscillations imply that there exist three distinct neutrino mass eigenstates possessing definite neutrino masses, $m_i$ ($i$=1, 2, 3), which are non-degenerate, namely, $m_i \neq m_j$ for $i \neq j$. This in turn implies that at least two neutrino species must be massive. In such a non-degenerate neutrino mass spectrum, each known flavor eigenstate, ($\nu_e$, $\nu_\mu$, $\nu_\tau$), linked to three respective charged leptons ($e, \mu, \tau$) via the charged current interactions, can be regarded as a non-trivial mixture of the neutrino mass eigenstates as

$$\begin{pmatrix} \nu_e \\ \nu_\mu \\ \nu_\tau \end{pmatrix} = U_{\mathrm{PMNS}} \begin{pmatrix} \nu_1 \\ \nu_2 \\ \nu_3 \end{pmatrix}, \tag{1}$$

where $\nu_i$ ($i$=1, 2, 3) denote the mass eigenstates, and $U_{\mathrm{PMNS}}$ is the so called *Pontecorvo-Maki-Nakagawa-Sakata* (PMNS) [7, 8] matrix, a $3\times3$ unitary matrix describing neutrino mixing. The first mass eigenstate $\nu_1$ is defined as the one with the largest portion of the electron flavor eigenstate $\nu_e$. The mixing matrix for antineutrinos is a complex conjugate of the one for neutrinos, $U_{\mathrm{PMNS}} \to U_{\mathrm{PMNS}}^*$. The standard parametrization of the PMNS matrix is given by [6]

$$U_{\mathrm{PMNS}} = \begin{pmatrix} 1 & 0 & 0 \\ 0 & c_{23} & s_{23} \\ 0 & -s_{23} & c_{23} \end{pmatrix} \begin{pmatrix} c_{13} & 0 & s_{13}e^{-i\delta_{CP}} \\ 0 & 1 & 0 \\ -s_{13}e^{i\delta_{CP}} & 0 & c_{13} \end{pmatrix}$$
$$\times \begin{pmatrix} c_{12} & s_{12} & 0 \\ -s_{12} & c_{12} & 0 \\ 0 & 0 & 1 \end{pmatrix} \begin{pmatrix} e^{i\eta_1} & 0 & 0 \\ 0 & e^{i\eta_2} & 0 \\ 0 & 0 & 1 \end{pmatrix}, \tag{2}$$

where the notation $c_{ij} \equiv \cos\theta_{ij}$ and $s_{ij} \equiv \sin\theta_{ij}$ is used. The $\delta_{CP}$ phase, whose non-zero value would induce a violation of the charge conjugation parity (*CP*) symmetry, is often called the Dirac *CP* phase. Here, $\eta_i$ ($i = 1, 2$) are the Majorana *CP* phases, which are physical only if neutrinos are Majorana-type particles but play no role in neutrino oscillations [9].

As shown later, a total of six parameters are needed to fully describe neutrino oscillations, namely, three mixing angles, one Dirac *CP* phase, and two independent mass squared differences. The latter characterize the degree of non-degeneracy of neutrino masses and are defined as

$$\Delta m_{ij}^2 \equiv m_i^2 - m_j^2 \quad (i, j = 1, 2, 3, i > j). \tag{3}$$

As will be discussed in detail in this publication, among these six parameters, the Jiangmen Underground Neutrino Observatory (JUNO) can significantly improve the precision of $\Delta m_{31}^2$ (or equivalently $\Delta m_{32}^2$), $\Delta m_{21}^2$, and $\sin^2\theta_{12}$. In addition, JUNO can measure $\sin^2\theta_{13}$ but with less precision than current reactor experiments [10–12], and is insensitive to $\sin^2\theta_{23}$ and $\delta_{CP}$.

### B.  Today's knowledge on oscillation parameters

Table 1 presents the current precision of the four mixing parameters within the reach of JUNO as obtained from the 2020 Review of Particle Physics [6], which is referred to as PDG2020. The mass ordering (MO) of neutrinos is still unknown, meaning that the sign of $\Delta m_{32}^2$ can be positive or negative. The normal mass ordering (NMO) corresponds to $\Delta m_{32}^2 > 0$, and the inverted mass ordering (IMO) to $\Delta m_{32}^2 < 0$. The most recent global analyses [13–15] yield estimations that are consistent with the values shown in Table 1. Current precision on most oscillation parameters is in the order of a few percent.

### C.  New knowledge to be provided by JUNO

One of the main goals of JUNO [16, 17] is to determine the neutrino MO. This can be done by precisely measuring the interference in the reactor antineutrino oscillation probability driven by two independent mass squared differences, $\Delta m_{31}^2$ and $\Delta m_{32}^2$, as originally considered in Ref. [18]. Additional details on JUNO's MO determination can be found in Ref. [16], and an updated estimate is under preparation. JUNO's physics program also includes studies of neutrinos from the Sun [19], the atmosphere [20], supernovae [21, 22], and planet Earth [16], as well as explorations of physics beyond the SM [16].

JUNO's measurement of the oscillated reactor antineutrino spectrum at $\sim 52.5$ km will also enable an independent determination of the $\Delta m_{31}^2$, $\Delta m_{21}^2$, $\sin^2\theta_{12}$, and $\sin^2\theta_{13}$ oscillation parameters, which is the focus of this publication. Of these, the first three will be determined to significantly better than 1%, inaugurating a new era of precision in neutrino oscillation measurements [16, 23,

24]. Such extraordinary precision is expected to have a vast impact across different research fields including particle physics, astrophysics, and cosmology. For instance, it will enable more stringent tests of the standard three flavor neutrino mixing picture, such as probing the unitarity of the PMNS matrix [25–30], with the potential to discover physics beyond the SM. It will also have important implications for other experimental efforts, for example by reducing the parameter space in the search for leptonic *CP* violation [31, 32] and neutrinoless double beta decay [33–35]. The precise knowledge of the leptonic mixing matrix may reveal its most fundamental structure and provide important clues for identifying the theoretical mechanisms behind neutrino mass and mixing generation [36]. Finally, the new precision will allow using neutrinos as a more reliable tool or messenger to probe the deep interiors of astrophysical objects such as the Sun, supernovae, and planet Earth.

Important updates are made compared to the previous estimate [16] of JUNO's sensitivity to the $\Delta m_{31}^2$, $\Delta m_{21}^2$, $\sin^2\theta_{12}$, and $\sin^2\theta_{13}$ oscillation parameters. Here only eight nuclear reactors are considered at 52.5 km instead of the ten envisioned when the experiment was first conceived. Moreover, the final location and overburden of the experimental site are used, which have a slight impact on the baseline to the reactors and the cosmic muon rate. In contrast with Ref. [16], which assumed a flat systematic uncertainty on the energy scale, the nonlinearity model, and the reactor antineutrino spectral shape, here a realistic inverse beta decay (IBD) selection with an improved muon veto strategy is employed whose efficiency is assessed with state-of-the-art simulation software. Likewise, realistic assumptions on detector performance drawn from the experience of similar running experiments, bench-test measurements, and comprehensive simulation studies [37], are used. Background rates and uncertainties are updated using the latest simulation software and the most recent measurements on the radioactivity of the detector materials and its environment [38], and additional backgrounds that were originally left out are now considered. Matter effects are also considered. Finally, the expected constraints on the reactor antineutrino spectral shape from the satellite Taishan Antineutrino Observatory (TAO) [39] are employed. All these inputs are described in detail in the following sections.

The remainder of this publication is organised as follows. Sections II and III introduce the neutrino oscillation framework and the experimental setup of JUNO, respectively. Section IV provides the specifics related to reactor antineutrino detection and selection. Section V describes the methodology used to perform the oscillation analysis and parameter extraction, together with the main results. Section VI is dedicated to the conclusions.

**Table 1.**  Today's best knowledge of neutrino oscillation parameters within the reach of JUNO and their $1\sigma$ uncertainties, as reported in the PDG2020 [6]. The relative uncertainties (in %) are indicated in the last column. NMO (IMO) implies normal mass ordering (inverted mass ordering).

|  | PDG2020 | Relative Uncertainty ($1\sigma$) |
|---|---|---|
| $\Delta m_{32}^2$ (NMO) | $(2.453 \pm 0.034) \times 10^{-3}$ eV$^2$ | 1.4% |
| $\Delta m_{32}^2$ (IMO) | $-(2.546 \pm 0.037) \times 10^{-3}$ eV$^2$ | 1.5% |
| $\Delta m_{21}^2$ | $(7.53 \pm 0.18) \times 10^{-5}$ eV$^2$ | 2.4% |
| $\sin^2\theta_{12}$ | $0.307 \pm 0.013$ | 4.2% |
| $\sin^2\theta_{13}$ | $0.0218 \pm 0.0007$ | 3.2% |

## II. NEUTRINO OSCILLATION FRAMEWORK FOR JUNO

In the presence of non-degenerate neutrino masses and non-trivial mixing, neutrinos and antineutrinos undergo flavor oscillations when they propagate in vacuum or in matter. In this section, we present the neutrino oscillation framework used in the rest of this work.

### A. Neutrino oscillation in vacuum

The general $U_{\text{PMNS}}$-parameterization-independent expression of the $\nu_\alpha \to \nu_\beta$ neutrino oscillation probabilities in vacuum for ultra-relativistic neutrinos is given by [6]

$$
\begin{aligned}
\mathcal{P}(\nu_\alpha \to \nu_\beta) = &\delta_{\alpha\beta} - 4 \sum_{i>j} \Re\left(U_{\alpha i}^* U_{\alpha j} U_{\beta i} U_{\beta j}^*\right) \sin^2 \Delta_{ij} \\
&+ 2 \sum_{i>j} \Im\left(U_{\alpha i}^* U_{\alpha j} U_{\beta i} U_{\beta j}^*\right) \sin \Delta_{ij}.
\end{aligned} \tag{4}
$$

where $U_{\alpha i}$, $U_{\beta j}$, $U_{\alpha j}$, $U_{\beta i}$ (with $\alpha, \beta = e, \mu, \tau$ and $i, j = 1, 2, 3$ being the flavor and mass indices respectively) are PMNS matrix elements and

$$
\Delta_{ij} = \frac{c^3}{\hbar} \cdot \frac{\Delta m_{ij}^2 L}{4E} \simeq 1.267 \cdot \frac{\Delta m_{ij}^2}{\text{eV}^2} \cdot \frac{L/E}{\text{m/MeV}}. \tag{5}
$$

In the above expression, $\Delta m_{ij}^2$ are the mass squared differences defined in Eq. (3), $L$ is the distance traveled by the neutrino, $E$ is the neutrino energy, $c$ represents the speed of light, and $\hbar$ is the reduced Planck constant [6]. For antineutrinos, the mixing matrix elements in Eq. (4) are replaced by their complex conjugates, as mentioned before.

In this work, we are particularly interested in the case where $\alpha = \beta = e$ in Eq. (4), which yields the survival probability of electron antineutrinos. Invariance of the charge, parity and time reversal symmetry dictates that the survival probabilities are identical for neutrinos and antineutrinos and given by:

$$
\begin{aligned}
\mathcal{P}(\bar{\nu}_e \to \bar{\nu}_e) = &1 - \sin^2 2\theta_{12} c_{13}^4 \sin^2 \Delta_{21} \\
&- \sin^2 2\theta_{13}\left(c_{12}^2 \sin^2 \Delta_{31} + s_{12}^2 \sin^2 \Delta_{32}\right) \\
= &1 - \sin^2 2\theta_{12} c_{13}^4 \sin^2 \Delta_{21} \\
&- \frac{1}{2} \sin^2 2\theta_{13}\left(\sin^2 \Delta_{31} + \sin^2 \Delta_{32}\right) \\
&- \frac{1}{2} \cos 2\theta_{12} \sin^2 2\theta_{13} \sin \Delta_{21} \sin(\Delta_{31} + \Delta_{32}).
\end{aligned} \tag{6}
$$

The standard parametrization of the mixing matrix shown in Eq. (2) has been used. Note that in the third, fourth and fifth lines of the above equation, we have re-

formulated the survival probability to factor out the solar-dominated, atmospheric-dominated, and MO-sensitive terms, which appear in this order. Note also that there is no dependence on either $\sin^2 \theta_{23}$ or $\delta_{CP}$.

### B. Neutrino oscillation in matter

Even though matter effects are relatively small in JUNO compared to long-baseline oscillation experiments, it is necessary to account for them to extract the correct values of the mixing parameters. In fact, ignoring matter effects would lead to biases in $\Delta m_{21}^2$ and $\sin^2 \theta_{12}$ of about 1% and 0.2% [40], respectively. A complete treatment of the impact of matter effects in JUNO can be found in Refs. [40–42], and this section offers only a brief synopsis of the main points.

The effective Hamiltonian that is responsible for the antineutrino propagation in matter [43, 44] is given by

$$
\begin{aligned}
\widetilde{\mathcal{H}}_{\text{eff}} = &\frac{1}{2E}\left[U \begin{pmatrix} m_1^2 & 0 & 0 \\ 0 & m_2^2 & 0 \\ 0 & 0 & m_3^2 \end{pmatrix} U^\dagger - \begin{pmatrix} A & 0 & 0 \\ 0 & 0 & 0 \\ 0 & 0 & 0 \end{pmatrix}\right] \\
= &\frac{1}{2E}\left[\widetilde{U} \begin{pmatrix} \widetilde{m}_1^2 & 0 & 0 \\ 0 & \widetilde{m}_2^2 & 0 \\ 0 & 0 & \widetilde{m}_3^2 \end{pmatrix} \widetilde{U}^\dagger\right],
\end{aligned} \tag{7}
$$

where $\widetilde{U}$ and $\widetilde{m}_i$ stand, respectively, for the effective neutrino mixing matrix and the $i$-th neutrino mass in matter. The matter parameter $A$ can be expressed as

$$
A = 2\sqrt{2}\, G_{\text{F}} N_e E \simeq 1.52 \times 10^{-4}\ \text{eV}^2 \cdot Y_e \cdot \frac{\rho}{\text{g/cm}^3} \cdot \frac{E}{\text{GeV}}, \tag{8}
$$

where $G_{\text{F}}$ is the so-called Fermi constant, $N_e$ is the number density of electrons, $Y_e \simeq 0.5$ is the electron fraction per nucleon and $\rho = (2.45 \pm 0.15)\ \text{g/cm}^3$ is the estimated average matter density with its associated uncertainty, obtained for JUNO by considering that the antineutrino trajectory passes through both the crust and the sediment of the Earth. Note that the minus sign in front of $A$ denotes the charged-current matter potential of electron antineutrinos in matter.

In JUNO, where matter effects are relatively small, a constant matter density profile can be assumed and the survival probability can be written in an analogous form as in vacuum, by simply replacing the mass eigenvalues and mixing angles used in Eq. (6) by those in matter, which are indicated with a tilde placed over the corresponding quantities as

$$
\begin{aligned}
\mathcal{P}(\bar{\nu}_e \to \bar{\nu}_e) = &1 - \sin^2 2\widetilde{\theta}_{12}\, \tilde{c}_{13}^4 \sin^2 \widetilde{\Delta}_{21} \\
&- \sin^2 2\widetilde{\theta}_{13}\left(\tilde{c}_{12}^2 \sin^2 \widetilde{\Delta}_{31} + \tilde{s}_{12}^2 \sin^2 \widetilde{\Delta}_{32}\right) \\
= &1 - \sin^2 2\widetilde{\theta}_{12}\, \tilde{c}_{13}^4 \sin^2 \widetilde{\Delta}_{21}
\end{aligned}
$$

$$-\frac{1}{2}\sin^2 2\widetilde{\theta}_{13}\left(\sin^2 \widetilde{\Delta}_{31} + \sin^2 \widetilde{\Delta}_{32}\right)$$

$$-\frac{1}{2}\cos 2\widetilde{\theta}_{12}\sin^2 2\widetilde{\theta}_{13}\sin \widetilde{\Delta}_{21}$$

$$\times \sin(\widetilde{\Delta}_{31} + \widetilde{\Delta}_{32}), \tag{9}$$

where $\tilde{c}_{ij} \equiv \cos\widetilde{\theta}_{ij}$, $\tilde{s}_{ij} \equiv \sin\widetilde{\theta}_{ij}$, with $\widetilde{\theta}_{ij}\,(i, j = 1, 2, 3,\, i < j)$ being the effective mixing angles in $\widetilde{U}$ with the standard parametrization as in Eq. (2).

An exact calculation of the survival probability can be obtained by numerical derivations of the eigenvalues and eigenvectors of $\widetilde{\mathcal{H}}_{\text{eff}}$, in principle, for an arbitrary matter density profile along the neutrino trajectory. On the other hand, there are also several analytical approximations based on different expansion methods performed under the constant matter density assumption. For some approximated analytic formulae of $\mathcal{P}(\bar{\nu}_e \to \bar{\nu}_e)$ and effective mixing parameters in matter for JUNO, please refer to, for example, Refs. [40–42]. In the following sensitivity studies, both the exact calculation and analytical approximations were employed and found to produce consistent results.

### III.  JUNO EXPERIMENTAL SETUP

JUNO is a multipurpose experiment currently under construction in Southern China that will use a 20 kton liquid scintillator target to study neutrinos from a variety of natural sources as well as from nuclear reactors. Most reactor antineutrinos in JUNO will originate from 2 and 6 cores in the Taishan and Yangjiang nuclear power plants (NPPs), respectively. Both plants are located at a baseline of about 52.5 km, which was optimized for the best sens-

itivity to the neutrino MO and have a combined nominal thermal power of 26.6 GW$_{\text{th}}$. Knowledge of the unoscillated reactor antineutrino spectrum shape is important for JUNO, so a dedicated small satellite detector [39], called TAO, will be placed at about 30 m from one of the Taishan reactors to precisely measure it, serving as a data-driven input to constrain the spectra of the other cores. A schematic illustrating the location of both JUNO and TAO is shown in Fig. 1. The experiment's main detector and the reactors considered in the analysis are described in detail in the following Subsections.

In JUNO's location, the energy spectrum will be distorted by a slow (low frequency) oscillation driven by $\Delta m_{21}^2$ and modulated by $\sin^2 2\theta_{12}$, as well as by a fast (high frequency) oscillation driven by $\Delta m_{31}^2$ and modulated by $\sin^2 2\theta_{13}$, as shown in Fig. 2. JUNO will be the first experiment to observe these two oscillation modes simultaneously. As detailed later, fitting the data spectrum against the predicted spectrum distorted by standard neutrino oscillations enables measuring the $\Delta m_{31}^2$, $\Delta m_{21}^2$, $\sin^2 \theta_{12}$, and $\sin^2 \theta_{13}$ oscillation parameters. The oscillated spectrum in JUNO also changes subtly depending on the neutrino mass ordering, thus providing sensitivity to this parameter. As previously mentioned, this measurement is not addressed in this publication.

#### A.  The JUNO detector

The JUNO detector will be deployed in an underground laboratory under the Dashi hill to limit the cosmogenic background. The 650 m overburden with average rock density of 2.61 g/cm$^3$ will suppress the cosmic-ray muon flux to $4.1 \times 10^{-3}$/(s·m$^2$).

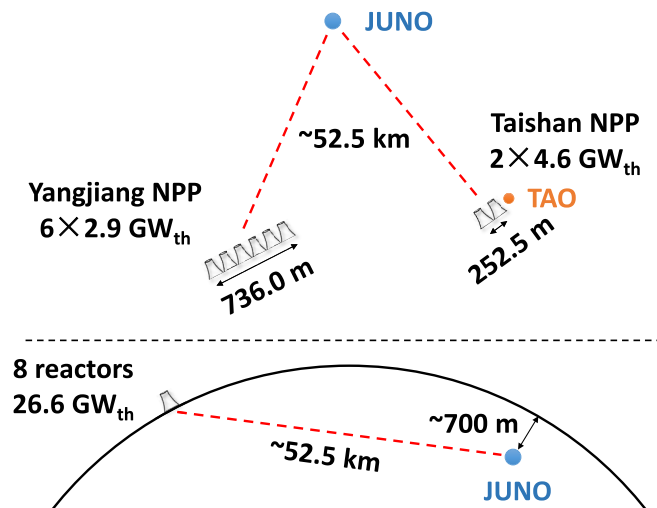The main JUNO detector is shown in Fig. 3. The



**Fig. 1.**   (color online) Setup of the JUNO experiment. The main 20 kton JUNO detector, indicated in blue, is located in an experimental cavern at a depth of about 700 m with respect to the surface and 650 m of overburden (1800 m.w.e), at a baseline of ~ 52.5 km from six 2.9 GW$_{\text{th}}$ reactor cores in the Yangjiang NPP and two 4.6 GW$_{\text{th}}$ cores in the Taishan NPP. The 2.8 ton TAO detector, indicated in orange, is located about 30 m away from one of the Taishan reactor cores.
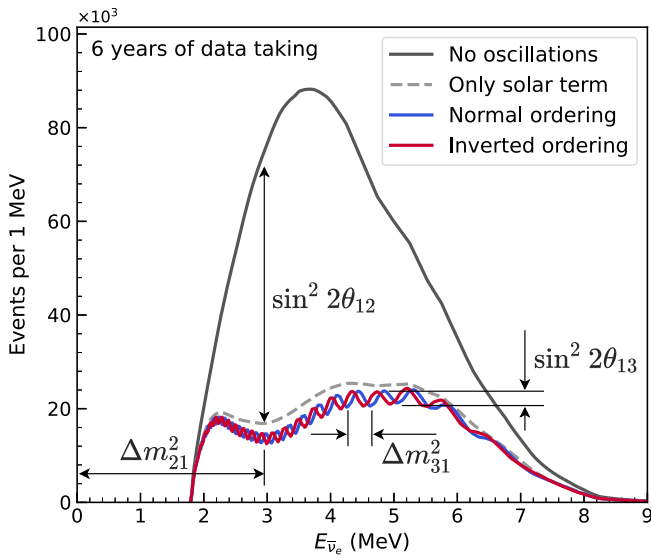
**Fig. 2.** (color online) JUNO reactor antineutrino energy spectrum without (black) and with (grey, blue and red) the effect of neutrino oscillation. The reactor spectra are convoluted with the IBD cross-section, whose threshold is 1.8 MeV, and assume 6 years of data-taking. The gray dashed curve shows the spectrum when only the term in the disappearance probability that is modulated by $\sin^2 2\theta_{12}$ is included, whereas the blue and red curves are obtained using the full oscillation probability in vacuum for the normal and inverted mass orderings, respectively. A detector with perfect energy resolution is assumed for illustration purposes. Some spectral features driven by the $\Delta m_{31}^2$, $\Delta m_{21}^2$, $\sin^2 2\theta_{12}$, and $\sin^2 2\theta_{13}$ oscillation parameters are shown pictorially, illustrating the rich information available in a high-resolution measurement of the oscillated spectrum at JUNO's baseline.

primary antineutrino target of 20 kton of liquid scintillator is contained in a transparent 12-cm thick acrylic sphere 35.4 m in diameter. This constitutes the largest detector of this kind, securing JUNO's desired antineutrino statistics. Disentangling the two oscillation modes requires the detector to have the ability to measure the fast atmospheric oscillations, for which an unprecedented energy resolution is required. The acrylic sphere is surrounded by 17612 large 20-inch photomultiplier tubes (PMTs), referred to as LPMTs, and 25600 small 3-inch PMTs, referred to as SPMTs, yielding an integral 77.9% photocathode coverage [17]. An ultra-pure water buffer with ~ 1.5 m thickness fills the volume between the acrylic and the LPMT photocathodes. The light yield at the detector center is expected to be ~ 1345 photoelectrons (PEs) per MeV [37]. This represents at least 2.5× more light compared to the second highest yield achieved with the same technology [45], and provides the required ≤ 3% at 1 MeV energy resolution for the MO determination [46]. The main detector is fully surrounded by an ultra-pure water Cherenkov detector that serves as both an

active veto for cosmic muons (efficiency >99.5%) and a passive shield against external radioactivity and neutrons from cosmic rays. The minimal thickness of this detector is 2.5 m. The muon cosmic veto system is supplemented with an external muon tracker consisting of three layers of plastic scintillator repurposed from the OPERA experiment [47] located at the top and providing a muon track angular reconstruction precision of 0.20°. This system covers about 60% of the surface above the water pool. More details about JUNO's detector design can be found in Ref. [17]. Discussion on the detector response, the corresponding systematic uncertainties, and their impact in this analysis, is deferred to Section IV.B.

**B. The JUNO nuclear reactors**

As shown in Fig. 1, the primary reactor antineutrino sources for JUNO are the Taishan and Yangjiang NPPs, with two and six cores respectively, located at an average distance of 52.5 km. The next closest reactor complex to JUNO is Daya Bay, whose antineutrino flux slightly reduces the sensitivity to the oscillation parameters and is thus considered in the analysis. The reactor power, baselines, and expected IBD rates from Taishan, Yangjiang, and Daya Bay reactor cores, are summarized in Table 2. The Huizhou NPP, at a distance of 265 km, is still under construction but will not be ready until several years after the start of data taking. Given the uncertainty on its schedule, it is not considered in the analysis. Other NPPs are more than 300 km away and contribute approx-

**Table 2.** Characteristics of NPPs and their reactor cores considered in this analysis: the two closest ones to JUNO, Taishan and Yangjiang, at an approximate distance of 52.5 km, and the next closest, Daya Bay. The IBD rates are estimated from the baselines, full thermal power of the reactors, selection efficiency, and current knowledge of the neutrino oscillation parameters. Relative contribution to the total antineutrino signal in JUNO is indicated in the last column.

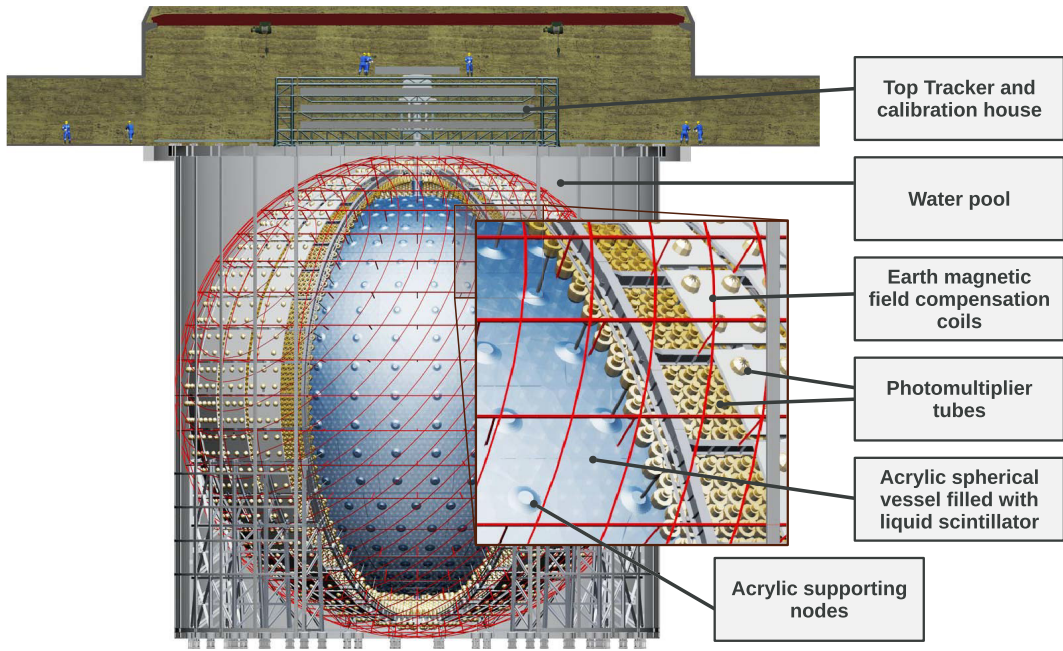| Reactor | Power /GW$_{th}$ | Baseline /km | IBD Rate /day$^{-1}$ | Relative Flux (%) |
|---|---|---|---|---|
| Taishan | 9.2 | 52.71 | 15.1 | 32.1 |
| Core 1 | 4.6 | 52.77 | 7.5 | 16.0 |
| Core 2 | 4.6 | 52.64 | 7.6 | 16.1 |
| Yangjiang | 17.4 | 52.46 | 29.0 | 61.5 |
| Core 1 | 2.9 | 52.74 | 4.8 | 10.1 |
| Core 2 | 2.9 | 52.82 | 4.7 | 10.1 |
| Core 3 | 2.9 | 52.41 | 4.8 | 10.3 |
| Core 4 | 2.9 | 52.49 | 4.8 | 10.2 |
| Core 5 | 2.9 | 52.11 | 4.9 | 10.4 |
| Core 6 | 2.9 | 52.19 | 4.9 | 10.4 |
| Daya Bay | 17.4 | 215 | 3.0 | 6.4 |

**Fig. 3.** (color online) Schematic of the main JUNO detector. An acrylic sphere containing 20 kton of liquid scintillator is immersed in water and surrounded by 17612 large (20-inch) and 25600 small (3-inch) inward-facing PMTs. This Central Detector is optically decoupled from a surrounding water pool instrumented with 2400 20-inch PMTs providing shielding and cosmic-ray muon tagging. A Top Tracker system consisting of three layers of plastic scintillator provides precision tracking of cosmic-ray muons entering the Central Detector. A calibration house is used to store the corresponding instruments deployed in the detector. Two sets of large coaxial coils running along different axes surround the Central Detector, largely suppressing the effects of the Earth's magnetic field on the 20-inch PMTs' collection efficiency.

imately one event per day to the total IBD rate in JUNO. As discussed in Section IV.A, they are treated as a background. More information on the reactor antineutrino flux prediction and the associated systematic uncertainties can be found in Section IV.C.

## IV. HIGH PRECISION REACTOR ANTINEUT-RINO DETECTION

### A. Reactor antineutrino selection and residual backgrounds

Reactor antineutrinos in JUNO are detected through the IBD reaction $\bar{\nu}_e + p \rightarrow e^+ + n$. The kinetic energy deposited by the positron via ionisation, together with its subsequent annihilation into typically two 0.511 MeV photons, forms a prompt signal. The impinging neutrino transfers most of its energy to the positron. This allows the deposited visible energy of the positron to be directly and very accurately related to the antineutrino energy, which is the relevant metric for neutrino oscillation measurements. The neutron is captured in an average of $\sim 220$ μs, and the corresponding photon emission forms a delayed signal. The neutron is captured dominantly on hydrogen ($\sim 99\%$), releasing a single 2.2 MeV photon, and very infrequently on carbon ($\sim 1\%$), yielding a

gamma-ray signal with 4.9 MeV of total energy. With a typical kinetic energy ranging from zero to a few tens of keV, the neutron in the IBD interaction carries only a small fraction of the initial antineutrino energy. However, due to the unprecedented energy resolution of JUNO, neutron recoils cannot be neglected, and the differential IBD cross-section is used in our calculations. We have adopted the IBD cross-section from Ref. [48], whose small uncertainty has no appreciable impact on the results presented in this publication.

The IBD prompt-delayed spatial and temporal coincidence signature can be mimicked by other events in the detector, giving rise to backgrounds. There are four main sources:

● Radiogenic events, i.e. $\alpha$, $\beta$, $\gamma$ decays from natural radioactivity in the material of the detector.

● Cosmogenic events, i.e. fast neutrons and unstable isotopes produced by impinging muons on $^{12}$C, typically via spallation.

● Atmospheric neutrinos, i.e. neutrinos of all flavors created in the reactions set about by the collision of primary cosmic rays with the Earth's atmosphere.

● Electron antineutrinos emitted by distant reactors or created in the U and Th decay chains in Earth, i.e. geoneutrinos.

The coincidence of two otherwise uncorrelated events, typically of radiogenic origin, forms the so-called accidental background. This background dominates the low energy part of the spectrum due to its nature. However, it can be measured with an excellent precision, typically at the permille level, and subtracted by off-time window techniques, as demonstrated by current-generation reactor antineutrino experiments [10–12].

Correlated backgrounds are by definition produced by a single physics process and yield both a prompt and a delayed signal. The most important such backgrounds are cosmogenic $^9$Li/$^8$He and fast neutrons, which can only be further suppressed by increasing the overburden. There are also geoneutrinos, mostly below 2.5 MeV in antineutrino energy [49], and atmospheric neutrinos [50]. The latter can produce neutrons, protons, $\alpha$ particles, and excited light nuclei that deposit their energy immediately or shortly after production and can thus mimic the IBD signature when followed by a neutron capture. There is only one radiogenic process leading to a correlated background deserving consideration: the $^{13}$C$(\alpha, n)^{16}$O reaction in the liquid scintillator. This background is expected to be small in JUNO, more so given the stringent radiopurity control that is envisaged [38]. The production of fast neutrons and gamma rays via spontaneous fissions and $(\alpha, n)$ reactions in peripheral materials of the detector [51] is expected to have a negligible contribution to this analysis.

IBD selection criteria are designed to suppress the aforementioned backgrounds while keeping a high efficiency for true reactor antineutrino IBD events. First, prompt and delayed candidate events are restricted to the energy windows [0.7, 12.0] MeV and [1.9, 2.5] ∪ [4.4, 5.5] MeV, respectively. IBD events are expected to dominate the [0.7, 8.0] MeV prompt energy range, as shown in Fig. 4. The delayed signal energy selection windows are selected to be centered around 2.2 MeV and 4.9 MeV, which correspond to neutron capture on hydrogen and carbon, respectively. Prompt or delayed events are discarded if their vertices are more than 17.2 m away from the detector center, since the external background rate is larger at the edge of the acrylic sphere. This fiducial volume cut will be further optimised upon data taking based on the final radiopurity of the PMTs and the detector materials. To further reduce the accidental background, the surviving prompt-delayed pairs are restricted to occur with a time separation $\Delta T_{p-d}$ smaller than 1.0 ms and a spatial 3D separation $\Delta R_{p-d}$ smaller than 1.5 m.

A series of cosmic muon veto cuts are enforced to suppress the cosmogenic backgrounds, most of which satisfy the IBD coincidence selection criteria. Muon-induced neutrons can be greatly reduced by imposing a time cut proportional to the characteristic time of neutron capture, as done in other underground liquid scintillator experiments [10– 12, 52]. However, this approach does not fully eliminate the longer-lived isotopes, in particular $^9$Li/$^8$He, that are produced along the muon track. The exploitation of this topological correlation has been considered by other experiments [52, 53]. A refinement of this strategy has been developed for JUNO with state-of-
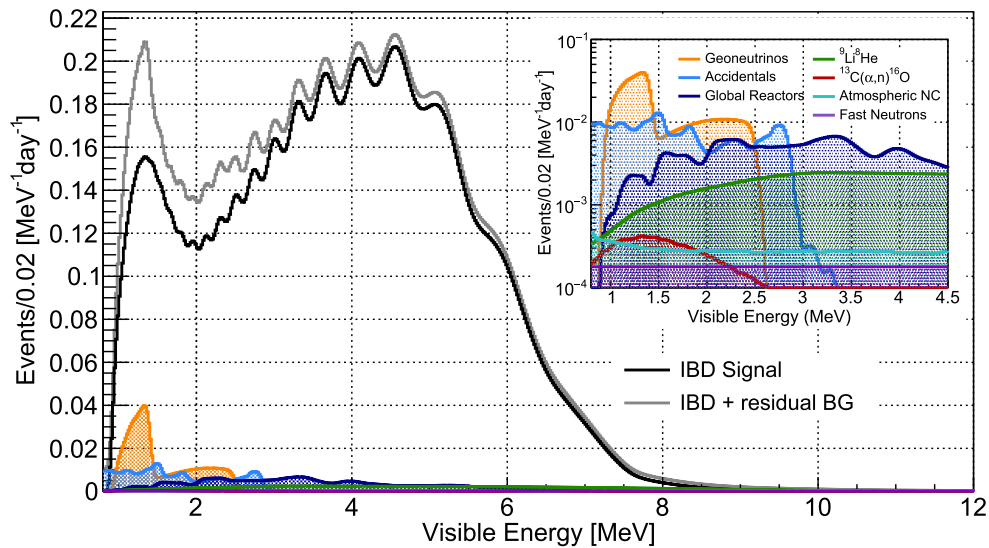


**Fig. 4.** (color online) Visible energy spectrum expected in JUNO as measured with the LPMT system with (grey) and without (black) backgrounds. The assumptions detailed in the text are used, which include the energy resolution from Ref. [37]. The inset shows the spectra of the expected backgrounds, which amount to about 7% of the total IBD candidate sample and are mostly localized below ~ 3 MeV.

the-art simulations by using a different veto time window depending on the candidate event's proximity to a recent muon track or spallation neutron capture. This strategy is a variation of the muon veto reported in Ref. [19], but optimized for the IBD selection. The details are as follows:

● For all muons passing the water pool Cherenkov detector and/or the Central Detector, a veto of 1 ms after each muon is applied over the whole fiducial volume to suppress spallation neutrons and short-lived radio-isotopes.

● For well-reconstructed muon tracks in the Central Detector caused by single or two far-apart muons, a veto of 0.6 s, 0.4 s, and 0.1 s is applied to candidate events with reconstructed vertices smaller than 1 m, 2 m, and 4 m away from the track(s), respectively.

● For events containing two close and parallel muons (< 3 m), which constitute roughly 0.6% of muon-related events, a single track is often reconstructed. The veto is applied around this track as described above, but the cylinder radii are increased according to their separation, which can be inferred from the charge pattern around the entrance and exit points.

● For events where a track cannot be properly reconstructed, which amount to about 2% of all muon-related events and occur primarily when more than two muons go through the detector simultaneously, a 0.5 s veto is applied over the whole fiducial volume.

● A 1.2 s veto is applied on any candidate events reconstructed inside a 3 m radius sphere around spallation neutron capture events. This cut helps further reject backgrounds from cosmogenic isotope decays.

Compared to Ref. [16], this updated strategy improves the muon veto efficiency from 83.0% to 91.6%, while reducing the residual $^9$Li/$^8$He background from 1.6 day$^{-1}$ to 0.8 day$^{-1}$. The combined antineutrino detection efficiency after all selection cuts is 82.2%. A rounded value of 82.0% was used in the analyses reported here. Breakdown of the selection efficiency is summarised in Table 3, where each component is found to be independent of neutrino energy. The IBD rate after event selection is 21% lower than Ref. [16], mainly as a result of the lesser number of reactors at 52.5 km (−26%), the updated reactor flux prediction of Sec. IV.C (−5%), the improved event selection efficiency (+13%), and smaller effects such as the updated baselines and the values of the other oscillation parameters.

After applying the antineutrino event selection cuts mentioned above, seven backgrounds remain that are

**Table 3.** Summary of cumulative reactor antineutrino selection efficiencies. The reported IBD rates refer to the expected events per day after the selection criteria are progressively applied. These rates are calculated for nominal reactor power, and do not include any reactor time off.

| Selection Criterion | Efficiency (%) | IBD Rate /day$^{-1}$ |
|---|---|---|
| All IBDs | 100.0 | 57.4 |
| Fiducial Volume | 91.5 | 52.5 |
| IBD Selection | 98.1 | 51.5 |
| Energy Range | 99.8 | – |
| Time Correlation ($\Delta T_{p-d}$) | 99.0 | – |
| Spatial Correlation ($\Delta R_{p-d}$) | 99.2 | – |
| Muon Veto (Temporal⊕Spatial) | 91.6 | 47.1 |
| Combined Selection | 82.2 | 47.1 |

**Table 4.** Background rates and uncertainties

| Background | Rate /day$^{-1}$ | Rate Uncertainty (%) | Shape Uncertainty (%) |
|---|---|---|---|
| Geoneutrinos | 1.2 | 30 | 5 |
| World reactors | 1.0 | 2 | 5 |
| Accidentals | 0.8 | 1 | negligible |
| $^9$Li/$^8$He | 0.8 | 20 | 10 |
| Atmospheric neutrinos | 0.16 | 50 | 50 |
| Fast neutrons | 0.1 | 100 | 20 |
| $^{13}$C($\alpha,n$)$^{16}$O | 0.05 | 50 | 50 |

considered in this analysis: geoneutrinos, $\bar{\nu}_e$'s from world reactors (with a baseline to JUNO larger than 300 km), accidental coincidences, $^9$Li/$^8$He decays, atmospheric neutrinos, fast neutrons, and $^{13}$C($\alpha$, $n$)$^{16}$O interactions. Their rates and uncertainties are summarized in Table 4. These values are consistent with those in our previous work [16], although some adjustments are made. The rates of geoneutrinos and $^9$Li/$^8$He decays are adjusted by +0.1 day$^{-1}$ and −0.8 day$^{-1}$, respectively, because of the new muon veto strategy. Likewise, the accidental background rate is reduced by 0.1 day$^{-1}$ due to new knowledge on the radiopurity of the detector components [38]. The world reactors and the atmospheric neutrino backgrounds are new additions in this publication. The former is calculated from Ref. [54] and the same uncertainty of the $\bar{\nu}_e$ signal described in Section IV.C is applied. The latter is estimated following the methodology of Ref. [50]. The IBD selection criteria is applied to simulate final states of atmospheric neutrinos interacting with $^{12}$C nuclei in the liquid scintillator. In the [0.7, 12.0] MeV energy range, neutral-current interactions are found to dominate, with charged-current interactions contributing a negligible amount. The uncertainty is estimated from the

largest variation in predicted rate between an interaction model that relies on GENIE 2.12.0, which is taken as the nominal, and four others relying on the NuWro generator that use different nuclear models and values of the axial mass [50].

The geoneutrino and world reactors' antineutrino spectra are obtained from Refs. [55] and [54], respectively. The accidental spectrum is obtained by applying the IBD selection to events from a full JUNO simulation with a recently re-estimated radioactivity budget [38]. The $^9$Li/$^8$He spectrum is obtained from a theoretical calculation. The atmospheric neutrino spectrum is the one produced by the nominal interaction model relying on the GENIE 2.12.0 generator in Ref. [50]. The fast neutron spectrum is assumed to be flat in the energy range of interest, which is a reasonable approximation as seen in both simulation and recent reactor experiments [11, 12, 56]. Finally, the spectrum of $^{13}$C($\alpha$, $n$)$^{16}$O is obtained from simulation [56]. In all cases the full detector response of Section IV.B is applied.

With the exception of the two newly considered backgrounds, the spectral shape uncertainties are the same as in Ref. [16]. The shape uncertainty of the world reactors' $\bar{\nu}_e$ background is considered to be the same of the $\bar{\nu}_e$ signal, described in Section IV.C. The spread between interaction models is assigned as the shape uncertainty of the atmospheric neutrino background. Like in other reactor experiments, many of the backgrounds will be estimated from data. In the absence of well-motivated models that can predict the correlations between bins in these empirical estimates, all shape uncertainties in this study are treated as bin-to-bin uncorrelated, which allows the spectra to vary in any way possible within the specified uncertainty envelopes. It was verified that introducing correlations between bins had a negligible impact on the sensitivity results.

Compared to other underground liquid scintillator experiments, the impact of the backgrounds on the precision of the measurement of the oscillation parameters is limited. This is because JUNO exploits the large spectral shape distortion of the IBD spectrum as the primary handle to extract the oscillation parameters. As illustrated in Fig. 4, the residual backgrounds' spectra are manifestly distinct from the oscillated spectrum.

## B. Detector response

The extraction of the oscillation parameters relies strongly on the careful control of systematic uncertainties affecting both the precision and accuracy of the spectral distortion caused by neutrino oscillation. The energy response model considered in this analysis includes three effects: energy transfer in the IBD reaction, detector nonlinearity, and energy resolution. The event-vertex dependence of the energy response, i.e. the non-uniformity,

also plays an important role and has been included in the energy resolution model as described below.

Energy transfer in the IBD reaction is calculated by integrating the IBD differential cross-section over the positron scattering angle. The kinetic energy of the positron, together with the energy of the typically two 0.511 MeV annihilation photons, is assumed to be fully deposited in the detector and is defined as $E_{\mathrm{dep}}$. Even though this work uses the full calculation, $E_{\mathrm{dep}}$ can be well approximated from the neutrino energy $E_\nu$ as $E_{\mathrm{dep}} \approx E_\nu + m_p - m_n + m_e \approx E_\nu - 0.782$ MeV, where $m_p$, $m_n$, and $m_e$ are the masses of the proton, neutron, and electron, respectively. Energy losses from escaping secondary gammas generated by Compton scattering and pair production only affect less than 1% of IBD events and are consequently ignored in this analysis. Due to the quenching effect of the scintillation light, the Cherenkov radiation, and the photon detection, the visible energy that would be observed if JUNO had perfect energy resolution, defined as $E_{\mathrm{vis}}^*$, does not depend linearly on the deposited energy [57]. For all events, $E_{\mathrm{vis}}^*$ is constructed by scaling the total number of detected photoelectrons with a fixed factor chosen so as to make $E_{\mathrm{vis}}^* = E_{\mathrm{dep}}$ for 2.2 MeV gammas released from neutron capture on hydrogen. Accordingly, the factor $E_{\mathrm{vis}}^*/E_{\mathrm{dep}}$ represents the nonlinear response of the detector, which is shown for positrons in the right top panel of Fig. 5. This curve crosses $E_{\mathrm{vis}}^*/E_{\mathrm{dep}} = 1$ at around 3 MeV instead of at 2.2 MeV because of the different nonlinearity between positrons and gammas. The fact that $E_{\mathrm{vis}}^*/E_{\mathrm{dep}} > 1$ above that energy does not mean that more energy is detected than is deposited, but rather that at those energies the photoelectron yield per MeV is higher than for neutron capture on hydrogen events. The instrumental charge nonlinearity of the JUNO LPMTs and their electronics is assumed to be negligible (<0.3%) thanks to the calibration done against the linear reference provided by the SPMTs, which operate primarily in photon-counting mode in the energy region of interest [37]. Therefore, in this analysis only the nonlinearity from the liquid scintillator itself is considered and assumed to be identical to the one measured in the Daya Bay experiment [57], whose scintillator composition is similar. The implementation of this systematic uncertainty in JUNO follows a similar strategy as in Daya Bay, where a nominal curve is first employed and four curves weighted by pull parameters are used to account for possible variations and to generate an uncertainty band, as shown in Ref. [57].

Finally, the visible energy $E_{\mathrm{vis}}$ is further smeared relative to $E_{\mathrm{vis}}^*$ because of the finite energy resolution of the detector. When detector leakage effects are neglected, which is an excellent approximation here given the large size of the detector and the use of a fiducial volume, the resolution can be parameterized using a Gaussian function with a standard deviation $\sigma_{E_{\mathrm{vis}}}$ given by
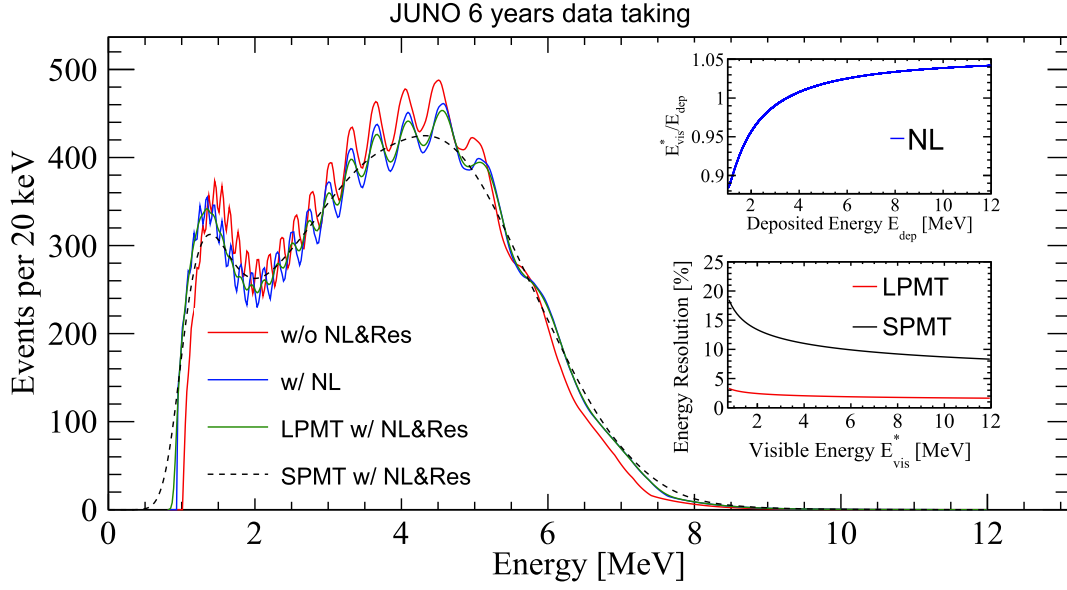
**Fig. 5.** (color online) Detector response impact on the prompt IBD signal spectrum. The top right panel shows the nonlinear energy response of the liquid scintillator. The bottom right panel shows the energy resolution of the LPMT and the SPMT systems as a function of visible energy. In both cases the resolution is described using the same model introduced in Eq. (10), with $a$=2.61%, $b$=0.82%, $c$=1.23% for LPMT and $a$=15.36%, $b$=0.82%, $c$=6.77% for SPMT. The main panel shows the deposited energy spectrum from the IBD reaction in 6 years of JUNO data without detector nonlinearity (NL) nor energy resolution (Res) in red, with NL only in blue, and with both detector effects in green, where the energy resolution corresponds to the LPMT system. The spectrum detected by the SPMT system with both NL and Res is also shown in dashed black.

$$\frac{\sigma_{E_{\text{vis}}}}{E_{\text{vis}}} = \sqrt{\left(\frac{a}{\sqrt{E_{\text{vis}}}}\right)^2 + b^2 + \left(\frac{c}{E_{\text{vis}}}\right)^2}, \qquad (10)$$

where $a$ is the term driven by the Poisson statistics of the total number of detected photoelectrons, $c$ is dominated by the PMT dark noise, and $b$ is dominated by the residual spatial non-uniformity of the detector. The large and small PMTs work as two complementary photon detection systems, resulting in the energy of every event being measured twice with very different resolutions. The energy resolution of the LPMT system was carefully studied using Monte Carlo simulation in Ref. [37], yielding $a = (2.61 \pm 0.02)\% \sqrt{\text{MeV}}$, $b = (0.82 \pm 0.01)\%$, and $c = (1.23 \pm 0.04)\% \text{MeV}$ as the average values for the fiducial volume of the detector. For the SPMT system, $a$ is expected to dominate because of the smaller light level, making $b$ and $c$ almost irrelevant. The value of this parameter is determined according to the ratio of the simulated total number of photoelectrons between the two PMT systems, while $c$ is calculated based on the measured dark noise rate of the SPMTs [58]. $b$ is not modified because detector effects are expected to be largely the same for both PMT systems. This results in $a = 15.36\% \sqrt{\text{MeV}}$, $b = 0.82\%$, and $c = 6.77\% \text{MeV}$ for the SPMT energy resolution. Despite the poorer energy resolution, the SPMT system allows for a semi-independent measurement of the slow $\Delta m_{21}^2$-$\sin^2 \theta_{12}$ oscillation, as explained in Section

V.C.

The energy spectrum at different stages in the calculation can be found in Fig. 5, embedded with the nonlinearity curve and the energy resolution curves of both PMT systems.

### C.   Reactor antineutrino flux

The expected visible energy spectrum observed at JUNO can be calculated as

$$S(E_{\text{vis}}) = N_p \cdot \epsilon \cdot \int_{T_{\text{DAQ}}} dt \int_{1.8\,\text{MeV}}^{12\,\text{MeV}} dE_{\bar{\nu}_e}$$
$$\cdot \Phi(E_{\bar{\nu}_e}, t) \cdot \sigma(E_{\bar{\nu}_e}) \cdot R(E_{\bar{\nu}_e}, E_{\text{vis}}), \qquad (11)$$

where $R(E_{\bar{\nu}_e}, E_{\text{vis}})$ is the detector energy response function embedding the effects described in Section IV.B that maps the antineutrino energy to the visible energy, $\sigma(E_{\bar{\nu}_e})$ is the IBD cross-section, $\Phi(E_{\bar{\nu}_e}, t)$ is the oscillated reactor antineutrino flux in JUNO at time $t$, $T_{\text{DAQ}}$ is the total data taking time, $\epsilon$ is the IBD event selection efficiency introduced in Table 3, and $N_p = 1.44 \times 10^{33}$ is the number of free protons in the detector target. Integration of the neutrino energy starts from the IBD reaction threshold at 1.8 MeV and ends at 12 MeV, where the reactor antineutrino flux is negligible.

In a commercial reactor, electron antineutrinos are produced from the fission products of four major iso-

topes, $^{235}$U, $^{238}$U, $^{239}$Pu, and $^{241}$Pu. The oscillated anti-neutrino flux at time $t$ is written as

$$\Phi(E_{\bar{\nu}_e}, t) = \sum_r \frac{\mathcal{P}_{\bar{\nu}_e \to \bar{\nu}_e}(E_{\bar{\nu}_e}, L_r)}{4\pi L_r^2} \phi_r(E_{\bar{\nu}_e}, t), \qquad (12)$$

where $E_{\bar{\nu}_e}$ is the $\bar{\nu}_e$ energy, $r$ is the reactor index, $L_r$ is the distance from the detector to reactor $r$, $\mathcal{P}_{\bar{\nu}_e \to \bar{\nu}_e}(E_{\bar{\nu}_e}, L_r)$ is the $\bar{\nu}_e$ survival probability, and $\phi_r(E_{\bar{\nu}_e}, t)$ is the reactor antineutrino energy spectrum. The latter can be calculated as

$$\phi_r(E_{\bar{\nu}_e}, t) = \frac{W_r(t)}{\sum_i f_{ir}(t) e_i} \sum_i f_{ir}(t) s_i(E_{\bar{\nu}_e}), \qquad (13)$$

where $W_r(t)$ is the thermal power, $e_i$ is the mean energy released per fission for isotope $i$, $f_{ir}(t)$ is the fission fraction, and $s_i(E_{\bar{\nu}_e})$ is the antineutrino energy spectrum per fission for each isotope. Averaged reactor power and fission fractions are used for this study, although these quantities will be provided by the power plants for each core as a function of time once JUNO begins operating. To account for refueling, which typically takes one month per year, the average reactor thermal power is calculated as the nominal value reduced by a reactor duty cycle factor of 11/12. The average fission fractions are assumed to be 0.58, 0.07, 0.30, 0.05, with mean energies per fission of 202.36 MeV, 205.99 MeV, 211.12 MeV, 214.26 MeV [59] for $^{235}$U, $^{238}$U, $^{239}$Pu, $^{241}$Pu, respectively. The $\bar{\nu}_e$ energy spectrum per fission of $^{235}$U, $^{239}$Pu and $^{241}$Pu is obtained from Huber [60], and of $^{238}$U from Mueller *et al.* [61].

Additional corrections are applied to account for the non-equilibrium and spent nuclear fuel contributions. The former arises from beta decays of some long-lived fission fragments and adds an extra ~0.6% to the antineutrino flux. The latter is caused by the spent nuclear fuel removed to cooling pools near the reactor cores still emitting antineutrinos and contributes an additional ~0.3% to the flux. The corrections are obtained from Ref. [62], both of which are assigned a 30% rate uncertainty and a negligible spectrum shape uncertainty, in agreement with the latest results from Daya Bay [10]. The total unoscillated spectrum for JUNO is obtained by aggregating the contributions of the four isotopes in the Huber-Mueller model and correcting for these two effects. Discrepancies have been found between the data and the models, most notably a ~5% deficit of the total flux with respect to the Huber-Mueller prediction, commonly known as the reactor antineutrino anomaly, and a spectral distortion in the ~[4,6] MeV region observed when comparing to both conversion and summation models [11, 12, 63–68]. Therefore, the ratio between the measurement and the total prediction in Daya Bay [62] is used to further cor-

rect the total prediction used in this sensitivity study.

The uncertainties of the predicted reactor antineutrino flux are listed at the top of Table 5. The baselines are known to 1 m, resulting in a negligible contribution to the flux uncertainty at distances of ~52.5 km. The reactor power data will be provided by the NPPs with an uncertainty of 0.5%. Likewise, the fission fractions will be provided with an uncertainty of 5%, which will contribute an uncertainty of 0.6% to the predicted number of events. The mean energy per fission is known precisely and contributes only a 0.2% uncertainty to the predicted number of events. Finally, a 2% correlated uncertainty is assigned for the mean cross-section per fission, which is the product of the IBD cross-section with the total antineutrino spectrum and is thus proportional to the number of predicted events. All of these uncertainties are drawn directly from the experience accumulated by the Daya Bay experiment [62].

As noted in Section III.A, TAO is a satellite detector

**Table 5.** Signal normalization systematic uncertainties of JUNO. All uncertainties (backgrounds included) are relative to the signal rate of 43.2 measured IBDs per day, which accounts for the reactors' duty cycle. These uncertainties are used as inputs to the analysis. The flux systematic uncertainties have correlated and uncorrelated terms with respect to the reactors. See the text for more details. The detection systematic uncertainties contain the same items of Table 3 plus the uncertainty on the number of target protons.

| Component | Input Uncertainty (%) |
|---|---|
| Flux | 2.2 |
|     Baseline (L) | - |
|     Energy per Fission | 0.2 |
|     Thermal Power (P) | 0.5 |
|     Fission Fraction | 0.6 |
|     Mean Cross-Section per Fission | 2.0 |
| Detection | 1.0 |
|     Fiducial volume (2 cm vertex bias) | 0.4 |
|     IBD Selection cuts | 0.2 |
|     Muon Veto | - |
|     Proton Number | 0.9 |
| Backgrounds | 1.0 |
|     Geoneutrinos | 0.8 |
|     $^9$Li/$^8$He | 0.4 |
|     Atmospheric neutrinos | 0.2 |
|     Fast neutrons | 0.2 |
|     $^{13}$C$(\alpha, n)^{16}$O | 0.1 |
|     Accidentals | <0.1 |
|     World reactors | <0.1 |

whose primary objective is to provide a precise and model-independent antineutrino spectrum for JUNO to use as a reference [39]. This spectrum will be measured with sub-percent energy resolution in most of the energy region of interest. The expected uncertainty from TAO's measured spectrum, estimated from a simulation of that detector [39], is propagated as the spectral shape uncertainty in this analysis. TAO will collect about two million IBD events in three years, representing 20 times the statistics of JUNO in six years. As a result, the statistical uncertainty with 20 keV-sized bins will be below 1% across the ~[2.5, 5.5] MeV energy range. The systematic uncertainties considered include the scintillator nonlinearity, differences in fission fractions, and the impact of using a fiducial volume cut. As will be shown in Fig. 6, the combined statistical and systematic uncertainties yield a spectral shape uncertainty that is below 1.5% in the [2, 4] MeV energy region. This energy-dependent uncertainty replaces the flat bin-to-bin uncertainty used in Ref. [16].

## V. NEUTRINO OSCILLATION ANALYSIS

To extract the neutrino oscillation parameters, we compare the nominal spectrum, a proxy of the expected spectrum that JUNO will measure, illustrated in Fig. 4, against the hypothesis model based on the standard parametrization ($\Delta m_{31}^2$, $\Delta m_{21}^2$, $\sin^2\theta_{12}$, and $\sin^2\theta_{13}$) described in Section II. The current section describes the procedure,

inputs, and systematic uncertainties used to perform this comparison, as well as the resulting sensitivities. The sensitivities' evolution with time, the correlations between oscillation parameters, and the impact of the systematic uncertainties on the parameters' precision, are also shown.

### A. Statistical method

To compare the data to the hypothesis model, we employ the least-squares method, and construct a binned $\chi^2$ with covariance matrices and/or pull terms to account for systematic uncertainties [69],

$$\chi^2 \equiv (\boldsymbol{M} - \boldsymbol{T}(\boldsymbol{\theta},\boldsymbol{\alpha}))^T \cdot \boldsymbol{V}^{-1} \cdot (\boldsymbol{M} - \boldsymbol{T}(\boldsymbol{\theta},\boldsymbol{\alpha})) + \sum_i \left(\frac{\alpha_i}{\sigma_i}\right)^2, \quad (14)$$

where $\boldsymbol{M}$ and $\boldsymbol{T}$ represent the measured and expected vectors of events per individual energy bin, respectively, and $\boldsymbol{V}$ is the covariance matrix of the prediction. For this analysis, $\boldsymbol{M}$ is set to the nominal expectation without any fluctuations. $\boldsymbol{T}$ depends on the oscillation parameters $\boldsymbol{\theta}$ described in Section II, as well as on the nuisance parameters $\alpha_i$, each of which has a corresponding systematic uncertainty $\sigma_i$. The pull terms on the right hand side of Eq. (14) can substitute any covariance matrix representing a systematic uncertainty, and vice-versa.

The full analysis, from the determination of $\boldsymbol{M}$ and $\boldsymbol{T}(\theta,\alpha)$ to the sensitivity calculations, was independently
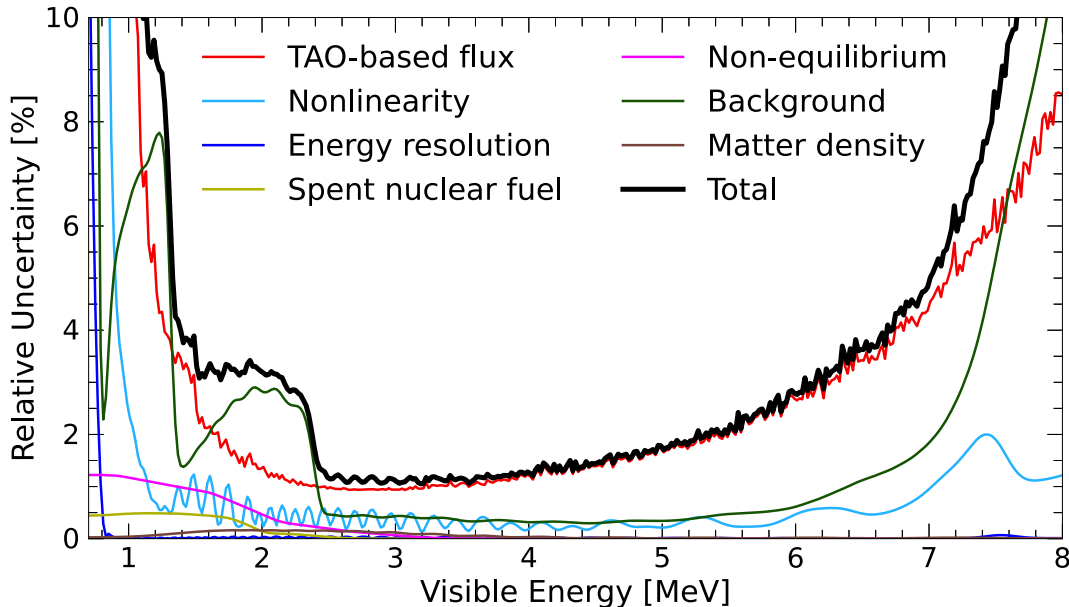


**Fig. 6.** (color online) Shape uncertainties relative to the number of events in each bin. These are obtained by generating simulated samples where systematic parameters are varied based on their assumed uncertainties and taking the ratio of the diagonal elements of the resulting covariance matrix to the number of nominal reactor antineutrino signal events in each bin. The rate uncertainties of the spent nuclear fuel and non-equilibrium corrections, as well as of the backgrounds, also distort the observed spectrum, and are consequently included in this figure. Square of the total uncertainty is the quadratic sum of all individual uncertainties.

carried out by four analysis groups that started from the same common inputs. These common inputs express the current best knowledge of JUNO's performance and reactor situation, as described in the previous sections, and are also used by other sensitivity studies within the JUNO collaboration. Each of the four groups chose a different strategy to perform the minimization of Eq. (14). One group used a covariance matrix-only approach, two groups used a pull term-only approach, and a fourth group used a mixture of both. Results were carefully compared at every stage of the analysis chain and differences in the final sensitivities were found to be much smaller than the systematic uncertainties. Accordingly, only one set of results, which is representative of the four groups, is shown in the remainder of this publication.

### B. Rate and shape systematic effects

The assessment of the systematic uncertainties benefits largely from the large pool of knowledge accumulated by past and current reactor experiments, particularly those focused on precisely measuring the $\theta_{13}$ mixing angle [10–12]. Systematic effects fall into two categories: rate and shape. Rate systematic uncertainties are those affecting the total number of IBD candidates (normalization), while shape systematic uncertainties are those that can bias the expected spectral shape (events per individual energy bin).

Rate systematic effects and their corresponding uncertainties are summarized in Table 5. They are divided into three main subcategories: flux, detection, and backgrounds. Within the flux subcategory, reactor-related uncertainties impact the analysis differently depending on whether they are correlated (2%) or uncorrelated (0.8%). Reactor correlated uncertainties, namely the mean cross-section per fission and energy per fission, affect all reactors contributing to the total neutrino flux in the same way, while reactor uncorrelated uncertainties, namely the thermal power and fission fraction, can vary independently from reactor to reactor. The detection systematic uncertainty of 1% encapsulates those uncertainties affecting the total number of selected IBD events. The dominant contribution on the flux category is the mean cross-section per fission, while on the detection category it is the target proton number uncertainty, which is estimated based on Daya Bay's experience [56]. The background rate uncertainties that are used as input to the analysis are shown in Table 4, but Table 5 shows the relative uncertainty of the background rates compared to the IBD signal rate so they can be compared to other rate systematic uncertainties. The relative impact of the various backgrounds is different in JUNO compared to short baseline reactor neutrino experiments because of the drastic difference in the signal to background ratio. The two dominant backgrounds in terms of their uncertainty relative to the IBD signal are geoneutrinos and $^9$Li/$^8$He, but their very

different spectral shapes compared to the distorted IBD spectra, illustrated in Fig. 4, provide additional constraints during the analysis.

The effects distorting the shape of the spectrum and their impact relative to the number of events are summarized in Fig. 6. The main contributions are the uncertainties in the reactor antineutrino spectrum and the backgrounds. As already mentioned in Section IV.C, there is mounting evidence that the systematic uncertainties of the predicted reactor antineutrino flux and shape are underestimated. For JUNO, the dedicated satellite detector TAO will provide the data-driven spectral uncertainty with an unprecedented energy resolution better than 2% at 1 MeV [39]. We use this TAO-based spectrum model uncertainty in our analysis. The uncertainty of the detector response model, described in Section IV.B and typically controlled to less than 0.5% [57, 70–72], is also important for the accuracy of the neutrino oscillation parameters. Its propagated uncertainty relates directly to the signal spectral shape, thus the small oscillations on Fig. 6. This figure also shows the background uncertainty with respect to the antineutrino signal, which includes all rate and shape uncertainties of Table 4. Similarly, the non-equilibrium and spent nuclear fuel uncertainties, discussed in the end of Section IV.C, are included in this figure, since they affect the signal spectrum in specific energy ranges. Finally, the 6% uncertainty on the matter density impacts the oscillation probability, as described in Section II.B, but makes a very small contribution to the shape uncertainty.

### C. Neutrino oscillation sensitivity results

The $1\sigma$ uncertainty for $\Delta m_{31}^2$, $\Delta m_{21}^2$, $\sin^2 \theta_{12}$, and $\sin^2 \theta_{13}$ is calculated with all rate and shape systematic uncertainties in three different regimes of data-taking time: 100 days (statistics-dominated regime); 6 years (nominal); and 20 years (systematics-dominated regime). Considering the reactor duty cycle factor of 11/12 introduced in Sec. IV.C, these correspond to about 92 days, 2009 days, and 6696 days of data taking with full reactor power, respectively. The $1\sigma$ limits of each parameter are obtained by marginalizing over all others, and finding the values for which $\Delta\chi^2$ changes by a unit. All analyses used 20 keV bins. This choice was the result of optimization studies showing that, while the sensitivity to the solar parameters is largely independent of the bin size, the sensitivity to the parameters driving the fast atmospheric oscillation still improves slightly when reducing the bin size to this width.

The total precision obtained is summarized in Table 6. Additionally, Fig. 7 shows the $\Delta\chi^2$ profiles of JUNO compared to today's state-of-the-art knowledge [6]. As shown there, JUNO is expected to improve upon today's precision by almost one order of magnitude for three out of six neutrino oscillation parameters, measur-

ing them to the per mille precision. In fact, about 100 days of data taking would be enough for JUNO to dominate the world precision on those parameters, although additional improvements are expected with more statistics.

This is particularly the case for $\Delta m_{31}^2$, as coarsely quantified in Table 6, but fully illustrated in Fig. 8 where the impact of the systematic uncertainties can be observed via the deviation of the total sensitivity from the statist-

**Table 6.** A summary of precision levels for the oscillation parameters. The current knowledge (PDG2020 [6]) is compared with 100 days, 6 years, and 20 years of JUNO data taking. No external constraint on $\sin^2\theta_{13}$ is applied for these results.

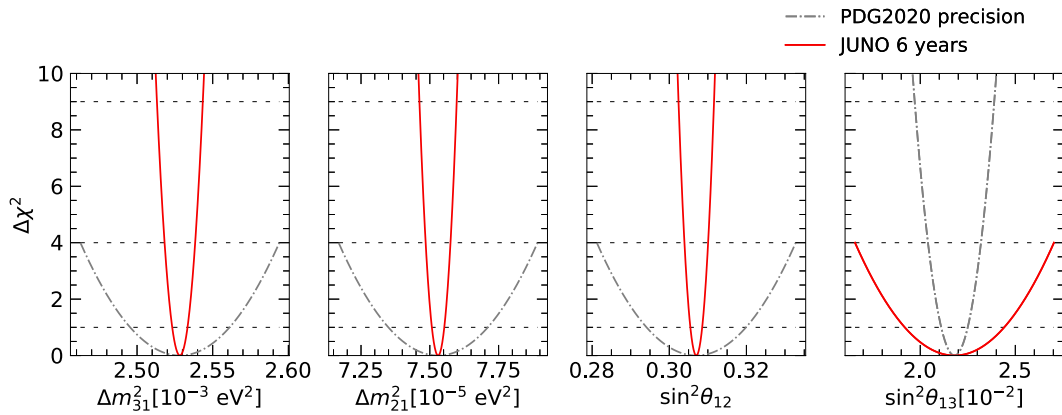|  | Central Value | PDG2020 | 100 days | 6 years | 20 years |
|---|---|---|---|---|---|
| $\Delta m_{31}^2$ ($\times 10^{-3}$ eV$^2$) | 2.5283 | ±0.034 (1.3%) | ±0.021 (0.8%) | ±0.0047 (0.2%) | ±0.0029 (0.1%) |
| $\Delta m_{21}^2$ ($\times 10^{-5}$ eV$^2$) | 7.53 | ±0.18 (2.4%) | ±0.074 (1.0%) | ±0.024 (0.3%) | ±0.017 (0.2%) |
| $\sin^2\theta_{12}$ | 0.307 | ±0.013 (4.2%) | ±0.0058 (1.9%) | ±0.0016 (0.5%) | ±0.0010 (0.3%) |
| $\sin^2\theta_{13}$ | 0.0218 | ±0.0007 (3.2%) | ±0.010 (47.9%) | ±0.0026 (12.1%) | ±0.0016 (7.3%) |



**Fig. 7.** (color online) Comparison of 1-d $\Delta\chi^2$ distributions of oscillation parameters: Today (PDG2020, dashed curve) v.s. projection with 6 years data taking of JUNO (solid red curve).
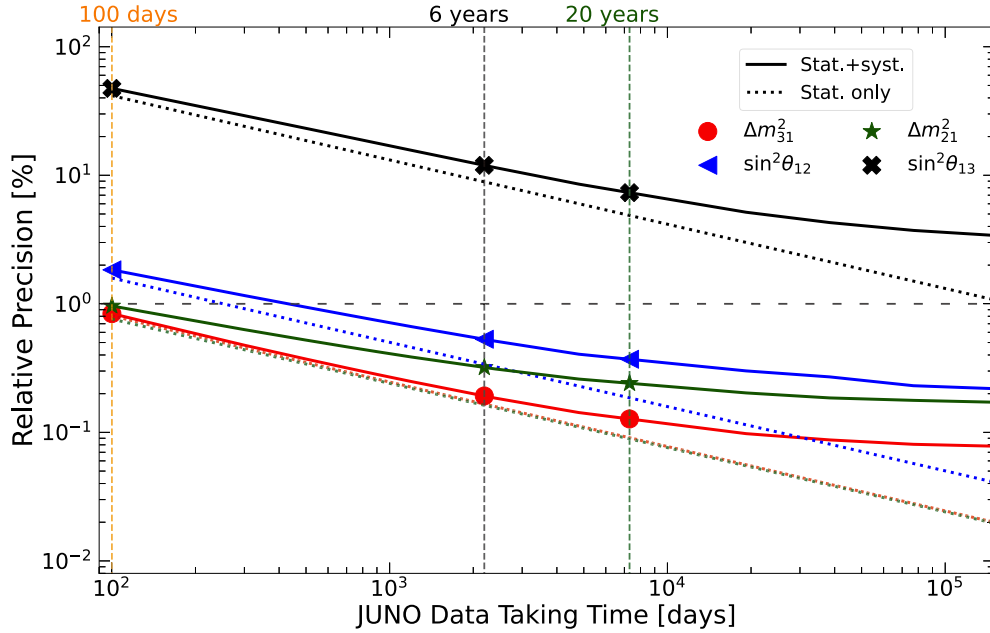


**Fig. 8.** (color online) Relative precision of the oscillation parameters as a function of JUNO data taking time. The markers and vertical lines stand for 100 days, 6 years, and 20 years of data taking. The horizontal gray dashed line stands for 1% relative precision. The green dotted and red dotted lines are on top of each other since the statistical-only precision is essentially identical for the $\Delta m_{31}^2$ and $\Delta m_{21}^2$ parameters.

ics-only limit.

The breakdown of statistical and systematic uncertainties on each parameter is shown in Fig. 9 for a nominal exposure of 6 years, allowing to identify the most important systematic effects. The statistics-only sensitivity is also provided so that the relative impact of the systematic uncertainties can be easily seen.

The sensitivity of the two mixing angles is dominated by rate systematic uncertainties, mainly from the reactor flux normalization and the detector efficiency, both of which affect the analysis in the exact same way. Rate uncertainties have dominated most measurements of oscillation parameters to date, but their impact here is mitigated by JUNO's rich spectral shape information that provides a constraint on the normalization. Even though the reactor correlated uncertainty (due to the mean cross-section per fission and energy per fission uncertainties) is roughly double the efficiency uncertainty as indicated in Table 5, their impact on the mixing angles is quite similar as seen in Fig. 9, differing by ~15% relative. In fact, if these uncertainties are increased very significantly, their impact on the precision changes very little from what it is shown.
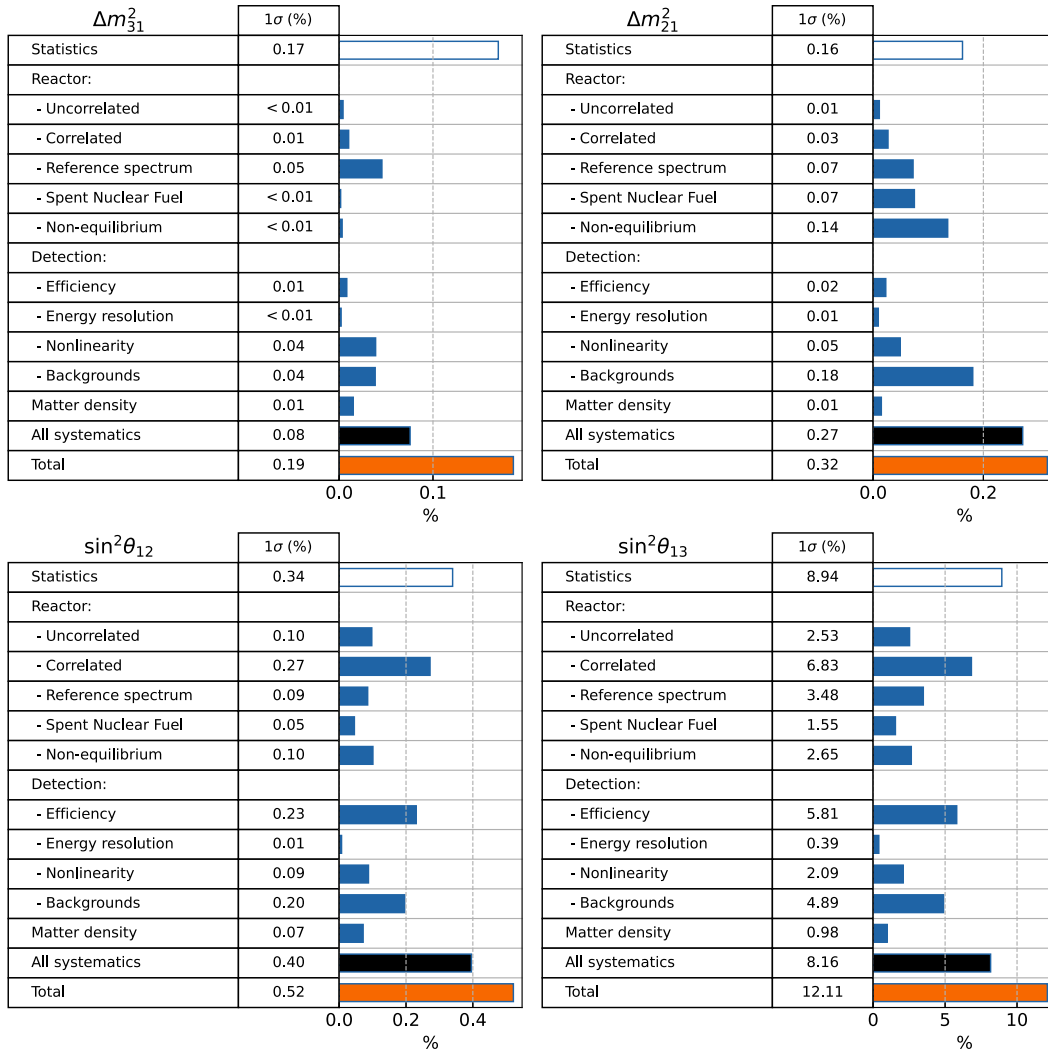
| $\Delta m_{31}^2$ | $1\sigma$ (%) |
|---|---|
| Statistics | 0.17 |
| Reactor: | |
|   - Uncorrelated | < 0.01 |
|   - Correlated | 0.01 |
|   - Reference spectrum | 0.05 |
|   - Spent Nuclear Fuel | < 0.01 |
|   - Non-equilibrium | < 0.01 |
| Detection: | |
|   - Efficiency | 0.01 |
|   - Energy resolution | < 0.01 |
|   - Nonlinearity | 0.04 |
|   - Backgrounds | 0.04 |
| Matter density | 0.01 |
| All systematics | 0.08 |
| Total | 0.19 |

| $\Delta m_{21}^2$ | $1\sigma$ (%) |
|---|---|
| Statistics | 0.16 |
| Reactor: | |
|   - Uncorrelated | 0.01 |
|   - Correlated | 0.03 |
|   - Reference spectrum | 0.07 |
|   - Spent Nuclear Fuel | 0.07 |
|   - Non-equilibrium | 0.14 |
| Detection: | |
|   - Efficiency | 0.02 |
|   - Energy resolution | 0.01 |
|   - Nonlinearity | 0.05 |
|   - Backgrounds | 0.18 |
| Matter density | 0.01 |
| All systematics | 0.27 |
| Total | 0.32 |

| $\sin^2\theta_{12}$ | $1\sigma$ (%) |
|---|---|
| Statistics | 0.34 |
| Reactor: | |
|   - Uncorrelated | 0.10 |
|   - Correlated | 0.27 |
|   - Reference spectrum | 0.09 |
|   - Spent Nuclear Fuel | 0.05 |
|   - Non-equilibrium | 0.10 |
| Detection: | |
|   - Efficiency | 0.23 |
|   - Energy resolution | 0.01 |
|   - Nonlinearity | 0.09 |
|   - Backgrounds | 0.20 |
| Matter density | 0.07 |
| All systematics | 0.40 |
| Total | 0.52 |

| $\sin^2\theta_{13}$ | $1\sigma$ (%) |
|---|---|
| Statistics | 8.94 |
| Reactor: | |
|   - Uncorrelated | 2.53 |
|   - Correlated | 6.83 |
|   - Reference spectrum | 3.48 |
|   - Spent Nuclear Fuel | 1.55 |
|   - Non-equilibrium | 2.65 |
| Detection: | |
|   - Efficiency | 5.81 |
|   - Energy resolution | 0.39 |
|   - Nonlinearity | 2.09 |
|   - Backgrounds | 4.89 |
| Matter density | 0.98 |
| All systematics | 8.16 |
| Total | 12.11 |

**Fig. 9.** (color online) An illustration of the relative impact of individual sources of uncertainty on the total precision of the $\Delta m_{31}^2$, $\Delta m_{21}^2$, $\sin^2\theta_{12}$, and $\sin^2\theta_{13}$ oscillation parameters. The empty boxes represent the uncertainty resulting from considering only the statistical uncertainty of the reactor antineutrino sample. The impact of each source of systematic error, represented by the filled blue boxes, is assessed by enabling the corresponding uncertainty together with the statistical uncertainty and removing the latter. The removal is done by assuming that the statistical and systematic uncertainties add in quadrature, which allows to isolate the systematic component as $\sqrt{(\text{stat.}+\text{syst.})^2 - (\text{stat.})^2}$. The filled black box on every graph is obtained using the same procedure but simultaneously turning on all sources of systematic uncertainty rather than one at a time. The total uncertainty resulting from simultaneously considering all sources of statistical and systematic error is shown in the last orange row of each table. All uncertainties correspond to six years of JUNO data and are reported as relative uncertainty contributions to the precision of the particular oscillation parameter.

As a matter of fact, JUNO will be the first oscillation experiment where the spectral information provides such a good constraint on the normalization.

On the other hand, the sensitivity to the two mass splittings is dominated by systematic uncertainties distorting the spectral shape, mainly those from the reference spectrum and the detector nonlinearity. The spent nuclear fuel, non-equilibrium, and background systematic effects also distort the spectral shape, particularly in the low energy region, impacting the precision of $\Delta m_{21}^2$. The precision of the $\Delta m_{31}^2$ and $\sin^2\theta_{13}$ parameters is statistics dominated even after six years of data taking, as indicated in Fig. 8.

Figure 9 also shows that the impact of the density uncertainty in the calculation of the matter effects is small. Nevertheless, it is important to consider this effect when fitting the oscillation parameters, since it impacts the central value of the measurement, as discussed in the beginning of Section II.B.

Table 6 and Fig. 8 show that JUNO alone has very

limited ability to constrain $\sin^2\theta_{13}$ beyond today's world knowledge. Notwithstanding, JUNO's independent measurement of this parameter will still be the first one at a baseline of ~52.5 km and will thus be a good test of the three-neutrino paradigm. If we constrain $\sin^2\theta_{13}$ with the uncertainty from PDG2020 [6], the relative improvement in the precision of the other three parameters is smaller than 0.3% with 6 years of data.

The impact of the neutrino mass ordering choice on the sensitivity of the parameters was also evaluated and found to be negligible. Therefore, the nominal results presented here are good for both the normal and inverted ordering hypotheses. Using the wrong ordering (e.g. using inverted ordering in a sample where normal ordering was assumed) produced sensitivities that are no larger than 5% of the nominal values.

As discussed in Section III.B, our nominal analysis considered the neutrino flux from the eight reactors ~52.5 km away from the JUNO detector, the six in the Daya Bay power plant and, as a background, all the other
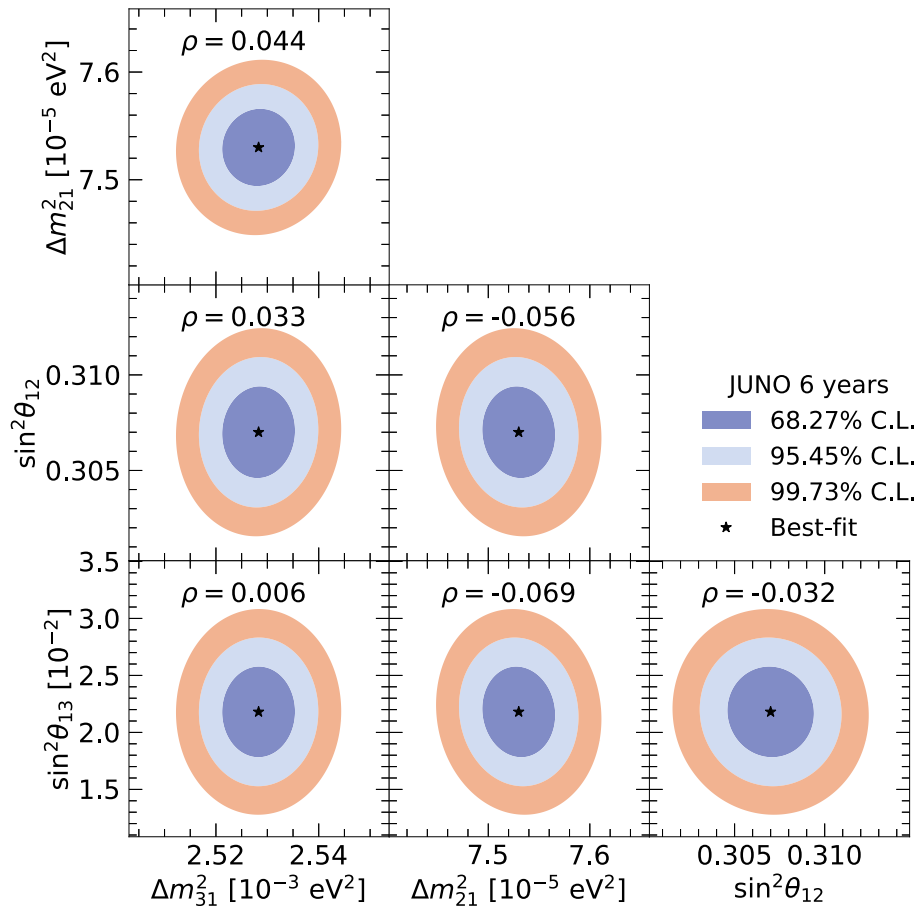


**Fig. 10.**    (color online) Two-dimensional 68.27%, 95.45%, and 99.73% confidence level (C.L.) contours for all pairs of oscillation parameters that JUNO is sensitive to. These contours correspond to the 1, 2, and 3$\sigma$ confidence regions, respectively. For each point in these projections, the underlying $\Delta\chi^2$ value is obtained by minimizing over the other two parameters. The black stars represent the best-fit points as well as the true values of the oscillation parameters. The correlation coefficient between each pair of oscillation parameters is shown as $\rho$.

reactors in the world. The flux from the Huizhou power plant was not included since no official date for its start of operations was available at the time of writing. However, assuming that the Huizhou power plant is operational from the beginning of JUNO data-taking reduces the sensitivities by less than a relative 3%.

Section III.A describes how JUNO has two independent PMT systems (SPMT and LPMT) for photo-detection with different photon occupancy regimes. The ability to perform a measurement of the oscillation parameters using only the SPMT system ($\sigma_E \sim 17\%$ for 1 MeV energy depositions) was also evaluated. While the measurement of the fast oscillation in Fig. 2 driven by $\sin^2 2\theta_{13}$ and $\Delta m_{31}^2$ requires a very good energy resolution, the solar parameters $\sin^2 2\theta_{12}$ and $\Delta m_{21}^2$ that drive the low frequency oscillation can be measured with the SPMT system alone (see Fig. 5). Using the simple model of Section IV.B to describe the energy resolution of this system, it was found that the expected precision of the two solar parameters is only less than 5% worse than the nominal results using the combined LPMT+SPMT system. This will provide a valuable internal validation of these parameters' measurement with some different systematic uncertainties, namely those uncorrelated across the two systems.

Finally, the stability and precision of the results are illustrated by the correlations between the oscillation parameters shown in Fig. 10. This figure depicts how these parameters are nearly uncorrelated, highlighting the abundant information available in JUNO's high-resolution measurement of the reactor antineutrino spectrum. It also explains the small impact of constraining $\sin^2 \theta_{13}$ as discussed above. Each parameter has a specific effect on the spectral shape that is retrievable with minimum interference between the parameters through the analysis described here.

## VI. CONCLUSION

JUNO is a next-generation liquid scintillator neutrino observatory under construction at a baseline of about 52.5 km from eight nuclear reactors in the south of China. Its unprecedented size and energy resolution will enable it to make a precise measurement of the oscillated spectrum of reactor antineutrinos and to observe the so-called solar and atmospheric effects simultaneously, resulting in the determination of the $\Delta m_{31}^2$, $\Delta m_{21}^2$, and $\sin^2 \theta_{12}$ oscillation parameters to significantly better than sub-percent precision. Updated sensitivities to these parameters have been obtained using the most recent information available to date about the experimental site's location and overburden, the detector response, the backgrounds, the surrounding nuclear reactors, and the reactor antineutrino spectral shape constraints expected from the TAO satellite detector. The sensitivities were assessed with four independent analyses using alternative but equally rigorous treatments of the systematic uncertainties, all of which yielded results in excellent agreement with each other. With six years of JUNO data taking, the $\Delta m_{31}^2$, $\Delta m_{21}^2$, and $\sin^2 \theta_{12}$ parameters will be determined to a precision of 0.2%, 0.3%, and 0.5%, respectively, which represents close to an order of magnitude improvement over existing constraints. These measurements will constitute an important input to other experiments, provide constraints for model building, and enable more precise searches for physics beyond the Standard Model in the neutrino sector.

## References

[1] C. Cowan, F. Reines, F. Harrison *et al*., Science **124**, 103 (1956)
[2] T. Kajita, Rev. Mod. Phys. **88**, 030501 (2016)
[3] A. B. McDonald, Rev. Mod. Phys. **88**, 030502 (2016)
[4] Q. R. Ahmad *et al*. (SNO), Phys. Rev. Lett. **89**, 011301 (2002), arXiv:nucl-ex/0204008
[5] Y. Fukuda *et al*. (Super-Kamiokande), Phys. Rev. Lett. **81**, 1562 (1998), arXiv:hep-ex/9807003
[6] P. Zyla *et al*. (Particle Data Group), PTEP **2020**, 083C01 (2020)
[7] B. Pontecorvo, Sov. Phys. JETP **26**, 984 (1968)
[8] Z. Maki, M. Nakagawa, and S. Sakata, Prog. Theor. Phys. **28**, 870 (1962)
[9] S. M. Bilenky, J. Hosek, and S. T. Petcov, Phys. Lett. B **94**, 495 (1980)
[10] D. Adey *et al*. (Daya Bay), Phys. Rev. Lett. **121**, 241805

(2018), arXiv:1809.02261
[11] H. de Kerret *et al*. (Double Chooz), Nature Phys. **16**, 558 (2020), arXiv:1901.09445
[12] G. Bak *et al*. (RENO), Phys. Rev. Lett. **121**, 201801 (2018), arXiv:1806.00248
[13] I. Esteban, M. Gonzalez-Garcia, M. Maltoni *et al*., JHEP **09**, 178 (2020), arXiv:2007.14792
[14] P. F. de Salas *et al*., JHEP **02**, 071 (2021), arXiv:2006.11237
[15] F. Capozzi *et al*., Phys. Rev. D **104**, 083031 (2021), arXiv:2107.00532
[16] F. An *et al*. (JUNO), J. Phys. G **43**, 030401 (2016), arXiv:1507.05613
[17] A. Abusleme *et al*. (JUNO), Prog. Part. Nucl. Phys. **123**, 103927 (2022)
[18] S. Petcov and M. Piai, Phys. Lett. B **533**, 94 (2002), arXiv:hep-ph/0112074
[19] A. Abusleme *et al*. (JUNO), Chin. Phys. C **45**, 023004

(2021), arXiv:2006.11760

[20] A. Abusleme *et al.* (JUNO), Eur. Phys. J. C **81**, 10 (2021), arXiv:2103.09908

[21] J.-S. Lu, Y.-F. Li, and S. Zhou, Phys. Rev. D **94**, 023006 (2016), arXiv:1605.07803

[22] A. Abusleme *et al.* (JUNO), *Prospects for Detecting the Diffuse Supernova Neutrino Background with JUNO*, (2022), arXiv: 2205.08830

[23] B. Abi *et al.* (DUNE), *Deep Underground Neutrino Experiment (DUNE)*, Far Detector Technical Design Report, Volume Ⅱ: DUNE Physics, (2020), arXiv: 2002.03005

[24] K. Abe *et al.* (Hyper-Kamiokande), *Hyper-Kamiokande Design Report,* (2018), arXiv: 1805.04163

[25] S. Antusch, C. Biggio, E. Fernandez-Martinez *et al.*, JHEP **10**, 084 (2006), arXiv:hep-ph/0607020

[26] S. Parke and M. Ross-Lonergan, Phys. Rev. D **93**, 113009 (2016), arXiv:1508.05095

[27] C. S. Fong, H. Minakata, and H. Nunokawa, JHEP **02**, 114 (2017), arXiv:1609.08623

[28] M. Blennow, P. Coloma, E. Fernandez-Martinez *et al.*, JHEP **04**, 153 (2017), arXiv:1609.08637

[29] Y.-F. Li, Z.-z. Xing, and J.-y. Zhu, Phys. Lett. B **782**, 578 (2018), arXiv:1802.04964

[30] S. A. R. Ellis, K. J. Kelly, and S. W. Li, JHEP **12**, 068 (2020), arXiv:2008.01088

[31] R. Acciarri *et al.* (DUNE), *Long-Baseline Neutrino Facility (LBNF) and Deep Underground Neutrino Experiment (DUNE)*: *Conceptual Design Report*, Volume 2: The Physics Program for DUNE at LBNF, (2015), arXiv: 512.061481

[32] K. Abe *et al.* (Hyper-Kamiokande Proto-), PTEP **2015**, 053C02 (2015), arXiv:1502.05199

[33] A. Dueck, W. Rodejohann, and K. Zuber, Phys. Rev. D **83**, 113010 (2011), arXiv:1103.4152

[34] S.-F. Ge and W. Rodejohann (JUNO and Neutrinoless Double Beta Decay), Phys. Rev. D **92**, 093006 (2015), arXiv:1507.05514

[35] J. Cao *et al.*, Chin. Phys. C **44**, 031001 (2020), arXiv:1908.08355

[36] S. F. King, *Theory Review of Neutrino Models and CP Violation*, in 19th Hellenic School and Workshops on Elementary Particle Physics and Gravity, 2019, arXiv: 1904.06660

[37] A. Abusleme *et al.* (JUNO), JHEP **03**, 004 (2021), arXiv:2011.06405

[38] A. Abusleme *et al.* (JUNO), JHEP **11**, 102 (2021), arXiv:2107.03669

[39] A. Abusleme *et al.* (JUNO), *TAO Conceptual Design Report: A Precision Measurement of the Reactor Antineutrino Spectrum with Sub-percent Energy Resolution*, (2020), arXiv: 2005.08745

[40] Y.-F. Li, Y. Wang, and Z.-z. Xing, Chin. Phys. C **40**, 091001 (2016), arXiv:1605.00900

[41] F. Capozzi, E. Lisi, and A. Marrone, Phys. Rev. D **89**, 013001 (2014), arXiv:1309.1638

[42] A. N. Khan, H. Nunokawa, and S. J. Parke, Phys. Lett. B **803**, 135354 (2020), arXiv:1910.12900

[43] L. Wolfenstein, Phys. Rev. D **17**, 2369 (1978)

[44] S. P. Mikheyev and A. Y. Smirnov, Sov. J. Nucl. Phys. **42**, 913 (1985)

[45] M. Agostini *et al.* (BOREXINO), Nature **587**, 577 (2020), arXiv:2006.15115

[46] Z. Djurcic *et al.* (JUNO), *JUNO Conceptual Design Report*, (2015), arXiv: 1508.07166

[47] T. Adam *et al.*, Detectors and Associated Equipment **577**, 523 (2007)

[48] P. Vogel and J. F. Beacom, Phys. Rev. D **60**, 053003 (1999)

[49] O. Šrámek, W. F. McDonough, and J. G. Learned, Adv. High Energy Phys. **2012**, 235686 (2012)

[50] J. Cheng, Y.-F. Li, L.-J. Wen *et al.*, Phys. Rev. D **103**, 053001 (2021), arXiv:2008.04633

[51] Z. Chen, X. Zhang, Z. Yu *et al.*, Phys. Rev. D **104**, 092006 (2021)

[52] S. Abe *et al.* (KamLAND), Phys. Rev. Lett. **100**, 221803 (2008), arXiv:0801.4589

[53] K. Abe *et al.* (Super-Kamiokande), Phys. Rev. D **94**, 052010 (2016), arXiv:1606.07538

[54] S. Dye and A. Barna, *Global Antineutrino Modeling for a Web Application*, (2015), arXiv: 1510.05633

[55] T. Araki *et al.*, Nature **436**, 499 (2005)

[56] F. P. An *et al.* (Daya Bay), Phys. Rev. D **95**, 072006 (2017), arXiv:1610.04802

[57] D. Adey *et al.* (Daya Bay), Nucl. Instrum. Meth. A **940**, 230 (2019), arXiv:1902.08241

[58] C. Cao *et al.*, Nucl. Instrum. Meth. A **1005**, 165347 (2021), arXiv:2102.11538

[59] X. B. Ma, W. L. Zhong, L. Z. Wang *et al.*, Phys. Rev. C **88**, 014605 (2013), arXiv:1212.6625

[60] P. Huber, Phys. Rev. C **84**, 024617 (2011), arXiv: 1106.0687, [Erratum: Phys. Rev. C **85**, 029901 (2012)]

[61] T. Mueller *et al.*, Phys. Rev. C **83**, 054615 (2011), arXiv:1101.2663

[62] F. An *et al.* (Daya Bay), Chin. Phys. C **41**, 013002 (2017), arXiv:1607.05378

[63] D. Adey *et al.* (Daya Bay), Phys. Rev. Lett. **123**, 111801 (2019), arXiv:1904.07812

[64] Y. J. Ko *et al.* (NEOS), Phys. Rev. Lett. **118**, 121802 (2017), arXiv:1610.05134

[65] M. Andriamirado *et al.* (PROSPECT), Phys. Rev. D **103**, 032001 (2021), arXiv:2006.11210

[66] H. Almazán *et al.* (STEREO), Phys. Rev. Lett. **125**, 201801 (2020), arXiv:2004.04075

[67] C. Giunti, Y. F. Li, C. A. Ternes *et al.*, Phys. Lett. B **829**, 137054 (2022), arXiv:2110.06820

[68] A. C. Hayes and P. Vogel, Ann. Rev. Nucl. Part. Sci. **66**, 219 (2016), arXiv:1605.02047

[69] D. Stump *et al.*, Phys. Rev. D **65**, 014012 (2001), arXiv:hep-ph/0101051

[70] E. Chauveau, *Calibration and Energy Scale in Double Chooz*, Zenodo (2018), 10.5281/zenodo.1314380

[71] A. Re, *Calibration and Energy Scale in Borexino*, Zenodo (2018), 10.5281/zenodo.1314410

[72] A. Gando, *Calibration and Energy Scale in KamLAND*, Zenodo (2018), 10.5281/zenodo.1314406